THE ASTROPHYSICAL JOURNAL, 507:113–130, 1998 November 1


# PROTOGALACTIC DISK MODELS OF DAMPED Lyα KINEMATICS

JASON X. PROCHASKA[1] AND ARTHUR M. WOLFE[1]
Department of Physics and Center for Astrophysics and Space Sciences, University of California, San Diego, C-0424, La Jolla, CA 92093
*Received 1998 March 36; accepted 1998 June 6*

## ABSTRACT

We present new observational results on the kinematics of the damped Lyα systems. Our full sample now comprises 31 low-ion profiles and exhibits characteristics similar to those of the sample from our previous paper.The primary exception is that the new distribution of velocity widths includes values out to a maximum of nearly 300 km $s^{-1}$, $\approx$100 km $s^{-1}$ greater than the previous maximum. These high velocity width systems will significantly leverage models introduced to explain the damped Lyα systems. Comparing the characteristics from low-redshift and high-redshift subsamples, we find no evidence for significant evolution in the kinematic properties of protogalaxies from $z = 2.0$ to $z = 3.3$.

The new observations give greater statistical significance to the main conclusions of our first paper. In particular, those models inconsistent with the damped Lyα observations in the first paper are ruled out at even higher levels of confidence. At the same time, the observations are consistent with a population of rapidly rotating thick disks (the TRD model) at high redshift, as predicted by cosmologies with early structure formation.

Buoyed by the success of the TRD model, we investigate it more closely by considering more realistic disk properties. Our goal is to demonstrate the statistical power of the damped Lyα observations by investigating the robustness of the TRD model. In particular, we study the effects of warping, realistic rotation curves, and photoionization on the kinematics of disks in the TRD model. The principal results are the following: (1) Disk warping has only a minimal effect on the kinematic results, primarily influencing the effective disk thickness. (2) The TRD model is robust to more realistic rotation curves; we point out, however, that the rotation curve derived from centrifugal equilibrium with H I gas alone does not yield acceptable results but that rather flat rotation curves such as those generated by dark matter halos are required. (3) The effects of photoionization require thicker disks to give consistent velocity width distributions.

*Subject headings:* galaxies: kinematics and dynamics — galaxies: structure — quasars: absorption lines

## 1. INTRODUCTION

This paper marks the third in a series of papers on the kinematics of the damped Lyα protogalaxies. These H I gas layers observed along sight lines to distant QSOs are widely believed to be the gaseous progenitors of modern galaxies (Wolfe 1995). Hence an examination of damped systems at high redshift provides insight into the process of galaxy formation. For instance, identifying the physical nature of these systems may distinguish between the monolithic collapse model (Eggen, Lynden-Bell, & Sandage 1962) and the hierarchical scenario favored by standard cosmogony. In our first paper (Prochaska & Wolfe 1997, hereafter PW), we demonstrated that the kinematics of damped Lyα systems at high redshift are consistent with these systems being thick, rapidly rotating disks; it is a description not unlike that predicted by monolithic collapse formation scenarios. At the same time, we found that damped Lyα systems cannot be simple exponential disks in a cluster normalized standard cold dark matter (CDM) cosmology (e.g., Kauffmann 1996). Subsequently, Jedamzik & Prochaska (1998) tightened this conclusion by considering a range of disk characteristics and CDM normalizations. They found that only a finely tuned disk model within the framework of CDM could be made marginally consistent with the damped Lyα observations. Recently, Haehnelt, Steinmetz, & Rauch (1997) have offered an alternative model for damped systems as gaseous protogalactic clumps undergoing infall within dark matter halos which may be consistent with the kinematic characteristics of the damped Lyα systems. Such a description lends itself naturally to the hierarchical cosmologies where merging plays a vital role. A future paper will address this model in greater detail. For the present work, we will focus on the interpretation of damped Lyα systems as thick rotating disks at high redshift.

In PW we analyzed the low-ion profiles from 17 damped Lyα systems and compared their kinematic characteristics with those of simulated profiles derived from several physical models. Of the models tested, we found the thick rotating disk model to be the only model consistent with the observations. The basic assumptions of the model are a flat rotation curve and an exponential gas distribution, both chosen to roughly correspond with the observations of local spiral galaxies. In this paper we present low-ion profiles for 14 additional damped systems. Therefore, our full kinematic sample consists of 31 low-ion profiles. We interpret the sample with disk models containing more physically realistic characteristics, e.g., disk warping and photoionization. We have two primary goals in mind: (1) to test the robustness of the interpretation of damped Lyα systems as disks and (2) to determine the effects on our conclusions regarding the thickness and rotation speed of these disks.

In § 2 we review the terminology and methodology introduced in PW. The new data are presented and tested against the models of PW in § 3. We investigate the effects of more realistic disk properties in § 4, and in § 5 we present a summary.

[1] Visiting Astronomer, W. M. Keck Telescope. The Keck Observatory is a joint facility of the University of California and California Institute of Technology.

## 2. A REVIEW

Our strategy is to compare the kinematic characteristics of low-ion profiles in damped Ly$\alpha$ systems with the simulated profiles derived from various physical models. In this manner, then, we investigate the agreement between the models and the damped systems. In this section we review the methodology and the thick rotating disk (TRD) model presented in PW.

To characterize the kinematics of the damped systems we focus on low-ion profiles such as Si II $\lambda$1808. After normalizing them to unit continuum strength, we create a binned apparent optical depth array, $\bar{\tau}(v)$, where $\bar{\tau}(v) = \langle \ln [I_c/I(v)] \rangle$, $I(v)$ is the intensity at velocity $v$, $I_c$ is the continuum intensity, and the average is taken over approximately two resolution elements centered at $v$. We focus on $\bar{\tau}(v)$ rather than $I(v)$ to minimize the effects of saturation, and we smooth in optical depth both to limit the effects of Poisson noise and to focus on broad features as opposed to individual components. Each profile is characterized by its signal-to-noise ratio (SNR), instrumental resolution, and peak optical depth ratio, $\bar{\tau}(v_{\rm pk})/\sigma(\bar{\tau})$, with $v_{\rm pk}$ the position of the maximum of $\bar{\tau}(v)$ in velocity space.

In PW, the only model considered that is consistent with the damped Ly$\alpha$ kinematic characteristics is the TRD model. For this model, we assume the following:

1. An exponential gas distribution,

$$n(R, Z) = n_0 \exp\left(-\frac{R}{R_d} - \frac{|Z|}{h}\right), \quad (1)$$

where $R$ and $Z$ are cylindrical radius and vertical displacement from the midplane, $n_0$ is the central gas density, $R_d$ is the radial scale length, and $h$ is the vertical scale height. Note that $n_0$ is related to the perpendicular column density at $R = 0$ by $N_\perp(0) = 2n_0\ h$.

2. A flat rotation curve parameterized by the rotation speed, $v_{\rm rot}$.

3. A random Gaussian velocity field parameterized by a one-dimensional velocity dispersion $\sigma_{\rm cc}$.

For the model systems considered here, we derive simulated profiles with identical SNR, instrumental resolution, and peak optical depth as the empirical data set. We employ the same Monte Carlo techniques as those used in § 3.2 of PW. However, we now consider 31 damped Ly$\alpha$ systems, which includes the 17 systems used in PW. To sample the model distributions sufficiently requires $\approx$10,000 sight lines; thus we perform 31 runs of 333 sight lines for every simulation. The SNR, $\bar{\tau}(v_{\rm pk})/\sigma(\bar{\tau})$, and instrumental resolution of the simulated profiles for each set of 333 sight lines is varied accordingly.

We quantify the kinematic characteristics of the profiles with four test statistics:

1. *Velocity interval test.*—The width of the profiles in velocity space, ($f_{\Delta v}$) or $\Delta v$. Formally, we calculate the total optical depth, $\tau_{\rm tot}$, of the profile in velocity space and define $\Delta v$ to be the velocity width encompassing $0.9\tau_{\rm tot}$ by trimming $0.05\tau_{\rm tot}$ off each edge of the profile.

2. *Mean-median test.*—Measures the asymmetry of the profile:

$$f_{\rm mm} = \frac{|v_{\rm mean} - v_{\rm median}|}{f_{\Delta v}/2}. \quad (2)$$

3. *Edge-leading test.*—Designates how edge-leading the peak of the profile is

$$f_{\rm edg} = \frac{|v_{\rm pk} - v_{\rm mean}|}{f_{\Delta v}/2}. \quad (3)$$

4. *Two-peak test.*—Designates how edge-leading the second peak of the profile is

$$f_{\rm 2pk} = \pm \frac{|v_{\rm 2pk} - v_{\rm mean}|}{f_{\Delta v}/2}. \quad (4)$$

In the above equations, $v_{\rm pk}$ and $v_{\rm 2pk}$ indicate the position of the peak and second strongest peak of the $\bar{\tau}(v)$ profile, and $v_{\rm mean}$ and $v_{\rm median}$ are the mean and median of the $\bar{\tau}(v)$ profile. We perform the statistical tests on the damped Ly$\alpha$ and simulated profiles in the same manner and compare the resulting distributions with the two-sided Kolmogorov-Smirnov (KS) test.

## 3. DAMPED Ly$\alpha$ PROFILES

### 3.1. *Data Samples and Selection Criteria*

The full kinematic data sample, designated sample B, comprises 17 damped Ly$\alpha$ systems from PW (sample A) and 14 new systems. Table 1 contains the journal of the 14 new observations. In Table 2 we list the following properties of the 14 new profiles: absorption redshift (col. [2]), log $N$(H I) (col. [3]), Fe abundance, i.e., log (Fe/H) $-$ log (Fe/H)$_\odot$ (col. [4]), Zn abundance (col. [5]), the low-ion transition (col. [6]), and $\bar{\tau}(v_{\rm pk})/\sigma(\bar{\tau})$ (col. [7]). From each new damped Ly$\alpha$ system we select a low-ion transition satisfying strict selection criteria. However, in order to include the highest redshift systems, we relax some of the selection criteria established in PW. This is because (1) the data have poorer SNR and (2) the high-$z$ systems have lower metallicity. Thus, even strong transitions (e.g., Fe II $\lambda$1608) are difficult to measure; for several of these damped systems no profile satisfies all the selection criteria of PW. Because we wish to maximize $\bar{\tau}(v)/\sigma(\bar{\tau})$ at the edge of each profile, in particular to ensure an accurate measurement of the velocity width, we adopt several profiles with peak normalized flux $I(v_{\rm pk})/I_c < 0.1$, which violates the previously established selection criterion (i.e., as in PW). In addition, we have relaxed the criterion that $\bar{\tau}(v_{\rm pk})/\sigma(\bar{\tau}) \geq 20$ on the grounds that numerical tests indicate this criterion was too conservative. In Figure 1 we present the velocity profiles as normalized intensity versus velocity, and in Figure 2 the corresponding binned optical depth arrays. Note that many of the new profiles (e.g., Q0019$-$15, Q1104$-$18) exhibit the same edge-leading asymmetry characteristic observed for the profiles of sample A. Furthermore, the distribution of profile widths resembles that of sample A, but the new distribution extends to 290 km s$^{-1}$, which exceeds the 200 km s$^{-1}$ maximum width in sample A. In fact, three of the 14 profiles have $\Delta v > 200$ km s$^{-1}$. The incidence of $\Delta v > 200$ km s$^{-1}$ in only one of 17 previous velocity profiles is due to small-number statistics.

Sample B includes two profiles with $I(v)/I_c < 0.1$, including one with $I(v)/I_c < 0.0$ where the flux falls below zero due to the effects of sky subtraction and Poisson noise. As emphasized in PW, the statistical tests used to characterize the profiles are sensitive to saturation; for example, a false determination of $v_{\rm pk}$ leads to incorrect values for all four statistical tests. We have strong reason to believe, however, that we are not contaminating the results by including these

TABLE 1

QSO AND OBSERVATIONAL DATA

| QSO | Date | Exposure Time (s) | $z_{em}$ | Resolution (km s$^{-1}$) | SNR | Date Set |
|---|---|---|---|---|---|---|
| Q0019−15..... | F96 | 35000 | 4.528 | 7.5 | 18 | W[a] |
| Q0347−38..... | F96 | 12600 | 3.23 | 7.5 | 33 | W |
| Q0951−04..... | S97 | 30600 | 4.369 | 7.5 | 13 | W |
| Q1005+36..... | S97 | 3600 | 3.17 | 7.5 | 12 | W[b] |
| Q1346−03..... | S97 | 31000 | 3.992 | 7.5 | 29 | W |
| Q1759+75..... | F96 | 10400 | 3.05 | 6.6 | 33 | W |
| Q2348−14..... | F96 | 9000 | 2.940 | 7.5 | 41 | W |
| Q0930+28..... | S97 | 17000 | 3.436 | 6.6 | 26 | SL[c] |
| Q1104−18..... | S97 | 19500 | 2.32 | 6.6 | 40 | SL |
| Q1850+40..... | S97 | 11880 | 2.120 | 6.6 | 16 | SL |
| Q2233+13..... | S97 | 15000 | 3.274 | 6.6 | 16 | SL |
| Q2343+12..... | S97 | 40000 | 2.58 | 6.6 | 35 | SL |
| Q2344+12..... | S97 | 15000 | 2.763 | 6.6 | 29 | SL |

[a] W: Data acquired by Wolfe & Prochaska.
[b] QSO coordinates kindly provided by R. H. Becker.
[c] SL: Data kindly provided by W. L. W. Sargent, L. Lu, and collaborators.

two profiles. First, in each case the profile has $I(v)/I_c < 0.1$ for only a few pixels. Therefore, the centroid of the peak is accurately determined to within a few km s$^{-1}$. Second, we can compare the saturated profiles with weaker, noisier, profiles from the same damped system. In Figure 3 we show this comparison. Note that the profiles track one another very closely, exhibiting nearly identical kinematic characteristics. Therefore, the kinematic results are not compromised by the minimal saturation evidenced in these two profiles. To calculate $\bar{\tau}(v)$ over the interval where $I(v)/I_c < 0.0$ we arbitrarily set $I(v)/I_c = \sigma(I)/2$ and calculate $\bar{\tau}(v)$ accordingly. Having performed numerical experiments that demonstrate that the original criteria were too strict, we establish a new set of saturation criteria: (1) the line profile must be free of blending with other absorption-line profiles, (2) the profile must not saturate for an excess of 1 resolution element, (3) the saturated region must not exceed one-fourth of the profile velocity width, and (4) $\bar{\tau}(v_{pk})/\sigma(\bar{\tau}) \geq 10$ instead of the previous value of 20. Together these criteria prevent an inaccurate determination of $v_{pk}$ and any resulting error in the test statistics.

To facilitate any parallel analysis performed with the damped Lyα surveys, where an accurate $N$(H I) is always measured (e.g., Wolfe et al. 1995), and to allow for the most accurate comparison with the Monte Carlo simulations, we construct a subset of sample B by imposing a stricter $N$(H I) criterion than that of PW. We refer to this subset of sample B as sample C. The criterion requires an $N$(H I) measurement for every damped system which must exceed $N_{thresh} = 2 \times 10^{20}$ cm$^{-2}$. This eliminates two systems from sample A (Q1946+60A and Q0449−13) inferred to be damped Lyα systems on account of their large ionic column densities, and one system (Q2212−16) with a measured $N$(H I) < $N_{thresh}$. In addition, the criterion eliminates Q2233+13 from the new systems. Therefore, sample C contains profiles from 27 damped systems. To investigate the evolution of the kinematic characteristics of the damped Lyα systems with redshift, we divide sample C at its median redshift and consider two subsets: (i) a low-redshift set of profiles with $\bar{z} = 2.06$ and $z_{median} = 1.96$ referred to as sample D and (ii) a high-redshift set of profiles with $\bar{z} = 3.24$ and $z_{median} = 3.35$ referred to as sample E. Table 3 summarizes the five data samples.

Figure 4 shows the statistical test distributions for samples A–E. The results for samples A and B are in good agreement, indicating that the addition of the new systems

TABLE 2

ADDITIONAL SAMPLE OF DAMPED Lyα SYSTEMS

| QSO | $z_{abs}$ | log $N$(H I) | [Fe/H] | [Zn/H] | Transition | $\bar{\tau}(v_{pk}/\sigma_{\bar{\tau}})$ |
|---|---|---|---|---|---|---|
| Q0019−15..... | 3.439 | 20.9 | > −1.7[a] | N/A | Fe II λ1608 | [b] |
| Q0347−38..... | 3.025 | 20.8 | −1.8 | N/A | Fe II λ1608 | 33 |
| Q0951−04A..... | 3.859 | 20.6 | −2.04 | N/A | Si II λ1526 | [b] |
| Q0951−04B..... | 4.203 | 20.4 | −2.94 | N/A | Si II λ1190 | 10 |
| Q1005+36..... | 2.799 | 20.6 | −2.0 | N/A | Fe II λ1608 | 13 |
| Q1346−03..... | 3.736 | 20.7 | < −1.7 | N/A | Si II λ1304 | 29 |
| Q1759+75..... | 2.625 | 20.8 | −1.27 | N/A | Si II λ1808 | 41 |
| Q2348−14..... | 2.279 | 20.6 | −2.35 | < −1.19 | Fe II λ1608 | 40 |
| Q0930+28..... | 3.235 | 20.3 | −2.03 | N/A | Fe II λ1608 | 31 |
| Q1104−18..... | 1.661 | 20.8 | −1.40 | −0.865 | Si II λ1808 | 44 |
| Q1850+40..... | 1.990 | 21.4 | −1.33 | −0.70 | Zn II λ2026 | 16 |
| Q2233+13..... | 3.149 | 20.0 | −1.5 | N/A | Fe II λ1608 | 19 |
| Q2343+12..... | 2.430 | 20.3 | −1.20 | N/A | Si II λ1808 | 25 |
| Q2344+12..... | 2.538 | 20.4 | −2.0 | N/A | Al II λ1670 | 36 |

[a] All limits are 3 σ limits.
[b] Profile is saturated at the peak.

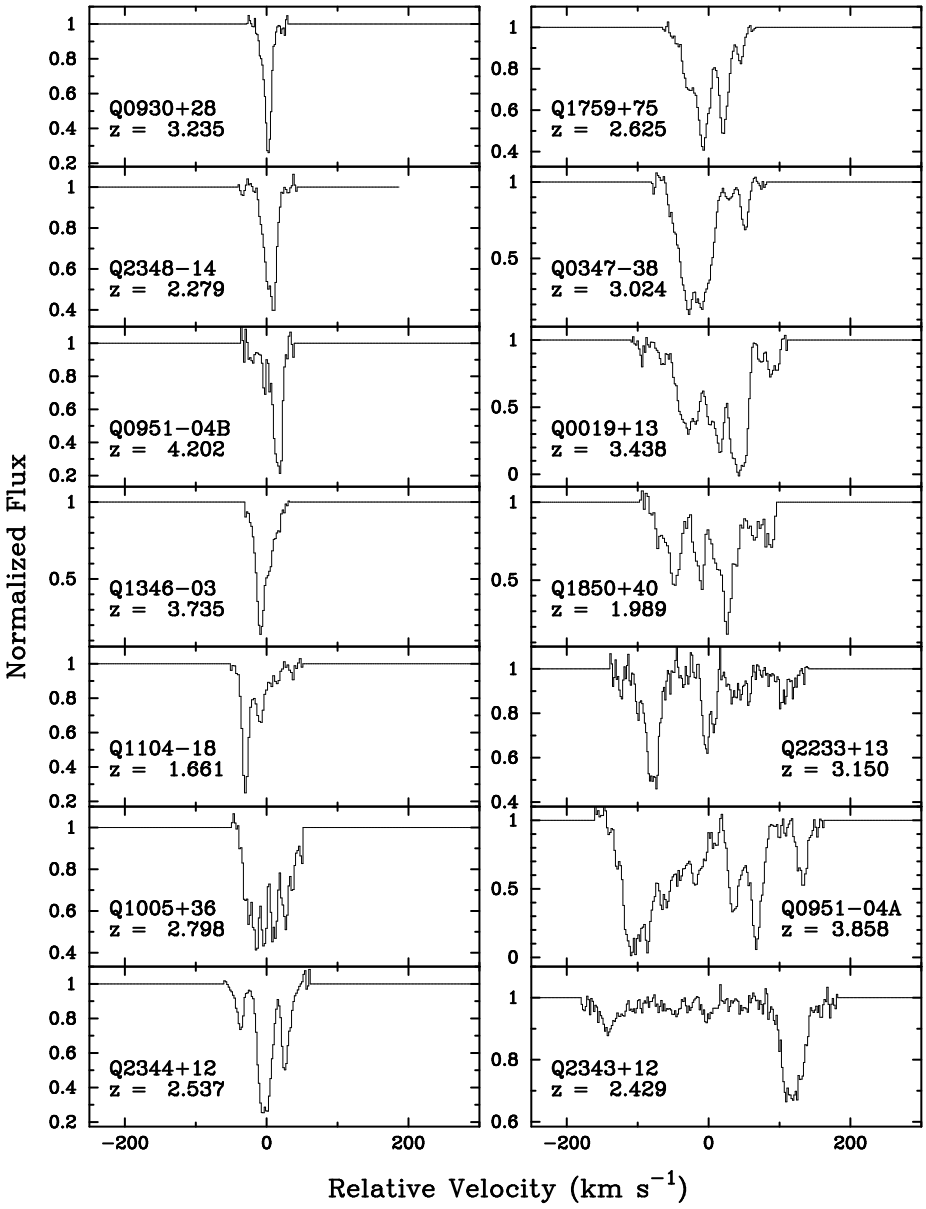


FIG. 1.—Velocity profiles of low-ion transitions for the 14 new damped Ly$\alpha$ systems. For each profile, $v = 0$ km s$^{-1}$ corresponds to the redshift labeled in the plot.

will serve to strengthen the conclusions of PW. The only significant difference between the two samples is the tail observed out to nearly 300 km s$^{-1}$ in the $f_{\Delta v}$ distribution of sample B. One also notes that samples B and C exhibit nearly identical distributions, therefore the stricter $N$(H I) criterion has little effect on our results. Similarly, the only disagreement observed by eye between samples D and E is in the mean-median test, but statistically the two distributions are consistent ($P_{KS} = 0.6$). We argue, therefore, that there is little evidence for an evolution of the kinematic characteristics with redshift. This will have significant impact on interpreting the damped Ly$\alpha$ systems in terms of the competing galaxy formation scenarios and will be further addressed in a future paper.

TABLE 3

DATA SAMPLES

| Sample | $N_{sys}$ | Comment |
|---|---|---|
| A ..... | 17 | Original selection criteria |
| B ..... | 31 | New selection criteria |
| C ..... | 27 | $N$(H I) measurement required |
| D ..... | 14 | Low-redshift cut of sample C |
| E ..... | 13 | High-redshift cut of sample C |

### 3.2. *Original Models Revisited*

Figure 5 presents the statistical test distributions for sample C as well as the distributions for seven of the Monte Carlo models presented in PW. The $P_{KS}$ values are the KS test probabilities that the model distribution and the corresponding distribution from sample C could have been drawn from the same parent population. The TRD1 model is the "best fit" to sample A. For this model, $h/R_d = 0.3$, $N_\perp(0) = 10^{21.2}$ cm$^{-2}$, and $v_{rot} = 225$ km s$^{-1}$, where $h$ is the vertical scale length, $R_d$ is the radial scale length, $N_\perp(0)$ is the central column density normal to the disk, and $v_{rot}$ is

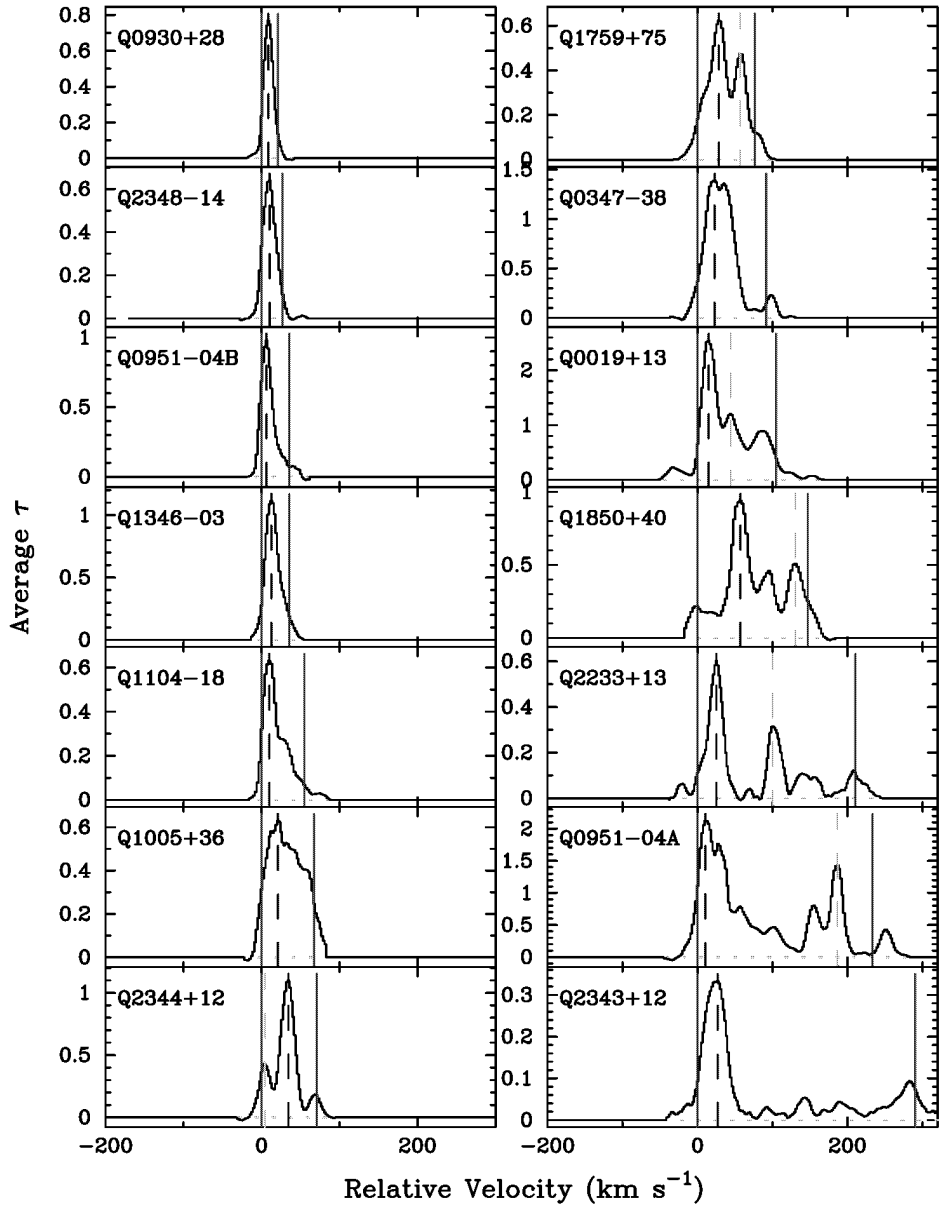


FIG. 2.—Average optical depth profiles (binned over 9 pixels) for the 31 transitions comprising our new total empirical data set. The solid vertical lines designate the velocity interval, $\Delta v$, while the dash-dotted lines indicate peaks and the dotted line is the $2\sigma(\bar{\tau})$ array. The profiles have been shifted in velocity space such that the left edge of the velocity interval coincides with $v = 0$, and reflected in about half the cases so that the strongest peak always lies on the left edge of the interval.

the flat rotation speed. The TRD2 model is identical to the TRD1 model except that $v_{\rm rot} = 300$ km s$^{-1}$. The remaining models are identical to those from § 6 of PW.

The addition of the new profiles has tightened the primary results of PW in every case. In particular, we point out the continued failure of every model except the TRD model to reproduce the damped Lyα observations. The TRD1 model is generally consistent with sample C, but because the model adopts the same rotation speed ($v_{\rm rot} = 225$ km s$^{-1}$) for all of the disks, it predicts no damped Lyα systems with velocity width $\Delta v > 250$ km s$^{-1}$. Hence, this simple model cannot reproduce the high-$\Delta v$ tail of the new empirical $f_{\Delta v}$ distribution. By contrast, the distribution from the TRD2 model extends to $\Delta v \approx 300$ km s$^{-1}$ and therefore provides a better match to the high-$\Delta v$ tail. Figure 6 plots the relative likelihood ratio test results for sample C against the TRD model with the central H I column density (*a*) $N$(H I) $= 10^{20.8}$ cm$^{-2}$, (*b*) $N$(H I) $= 10^{21.2}$ cm$^{-2}$, and (*c*) $N$(H I) $= 10^{21.6}$ cm$^{-2}$. The figure indicates a lower limit of $v_{\rm rot} > 250$ km s$^{-1}$ and that the optimal rotation speed is $v_{\rm rot} \approx 300$ km s$^{-1}$. However, if damped systems evolve to present galaxies, then a single population of disks with $v_{\rm rot} = 300$ km s$^{-1}$ is unacceptable, since such large rotation speeds are rarely observed. One concludes the single population disk model is too simple and must be revised. Models including distributions of rotation speeds and sight-line encounters with multiple disks will be considered in future papers. In this paper we retain the assumption of a single population of disks and study how more realistic disk properties affect the test statistic distributions.

## 4. IMPROVED DISK MODELS

In this section we improve on the TRD model by introducing more realistic disk characteristics. We test the TRD

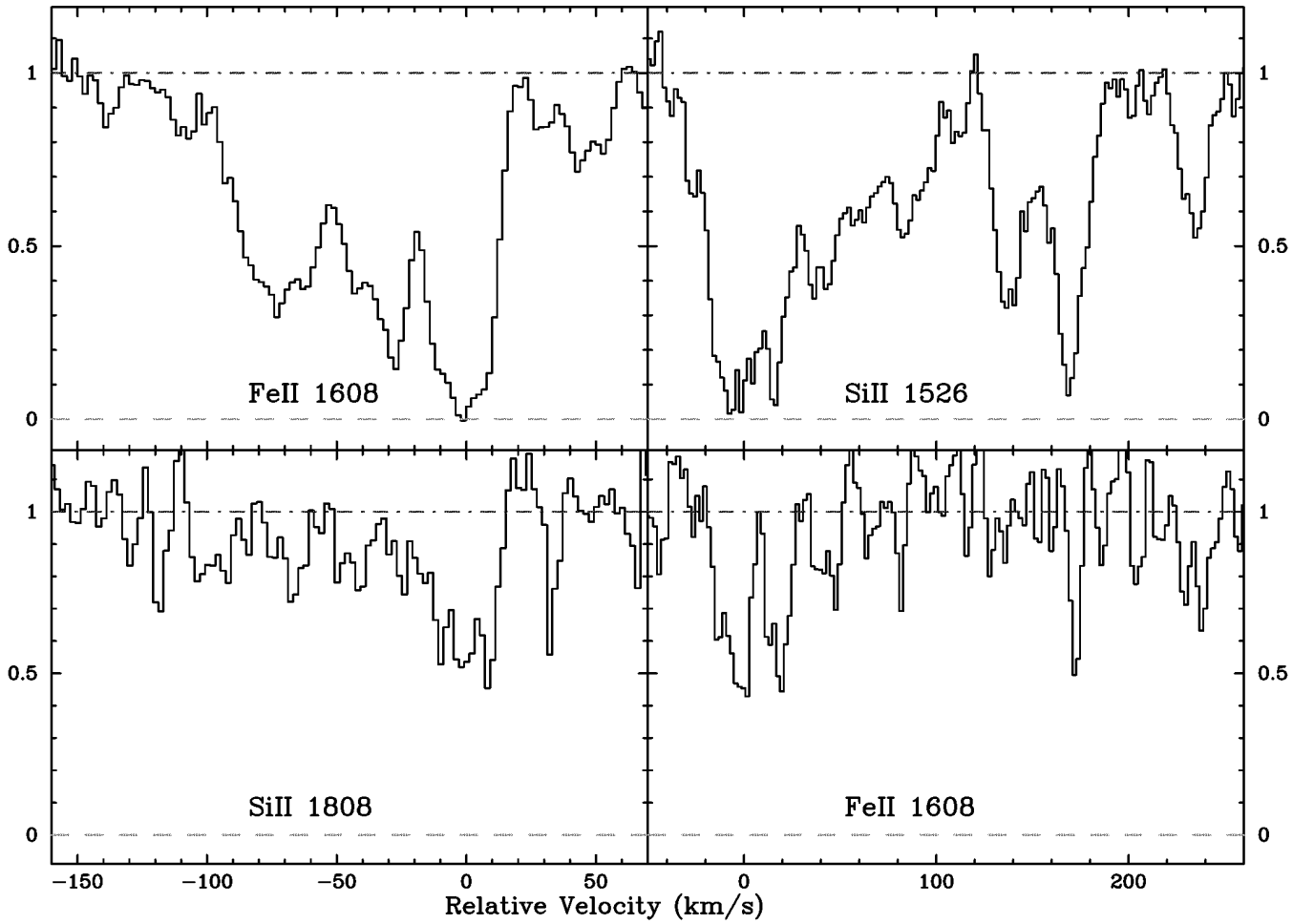


FIG. 3.—Comparison of a mildly saturated low-ion profile with a weak profile for the damped Ly$\alpha$ systems toward (*a*) Q0019−15 at $z = 3.439$ (*left*) and Q0951−04 at $z = 3.859$ (*right*). Note that the profiles track each other very closely and therefore exhibit nearly the same kinematic characteristics, irrespective of the saturation.

model against the damped Ly$\alpha$ observations in the light of these properties and thereby gauge the robustness of the model. The discussion focuses primarily on the velocity width test statistic because the other test statistics are less sensitive to changes in disk properties.

### 4.1. *The Warped-Disk Model*

H I 21 cm observations of local spiral galaxies (e.g., Briggs 1990) suggest that a significant fraction of disks are warped. Therefore, if the damped Ly$\alpha$ systems evolve into disk galaxies, as we have argued, the effects of warps must be considered. Warps produce two opposite kinematic effects: (i) some warped disks will have a large cross section to sight lines that satisfy $N(\mathrm{H\ I}) \geq 2 \times 10^{20}\ \mathrm{cm}^{-2}$ with large impact parameter and therefore small $\Delta v$. For instance, a tangent to the outer edge of a warped disk may have very large impact parameter (small $\Delta v$) yet still satisfy the $N$(H I) criterion (see Fig. 9*a* below), and (ii) those sight lines which doubly penetrate the disk (at a warped edge in addition to the unwarped inner disk; see Fig. 9*b*) will tend to yield larger $\Delta v$ than if they penetrated an unwarped disk. If the latter effect dominates, one expects a warped disk to yield a $f_{\Delta v}$ distribution with a greater number of large $\Delta v$ values, which imitates a thicker and/or more rapidly rotating unwarped disk. In some cases, however, we find that the former effect dominates the results, thereby lowering the median of the $f_{\Delta v}$ distribution.

Unlike the TRD model, the warped-disk model cannot be treated analytically. Standard modeling techniques involve decomposing the disk into a number of concentric rings, each with a unique orientation, with the configuration described by a "line of nodes." Figure 7*a* is a polar plot of a line of nodes where each successive point identifies rings with larger radii. We have used different symbols to help distinguish the points. The radial distance ($\alpha$) to each symbol indicates the tilt angle, and the azimuthal position ($\beta$) designates the position angle of the tilt axis. We define the reference plane by the orientation of the rings with smallest radius, i.e., the inner disk. Figures 7*b*–7*d* show three views of the warped disk corresponding to this line of nodes. In the following, we consider four lines of nodes characterized by $R_{\mathrm{H}}$, an effective Holmberg radius, which sets the radial separation of the rings. Figure 8 plots the lines of nodes with respect to $R_{\mathrm{H}}$. Included is a NULL line of nodes (Fig. 8*a*) describing an unwarped disk, the lines of nodes for M83 and M33 (Figs. 8*b* and 8*c*, respectively; Briggs 1990) and an artificially constructed line of nodes (CLON). Because we treat the warp model numerically, we will compare against the results of the null models and not the analytic TRD model in order to measure properly the consequences of warping without being biased by any numerical effects. Figure 9 illustrates the two kinematic effects mentioned above. In Figure 9*a* a sight line penetrates a disk

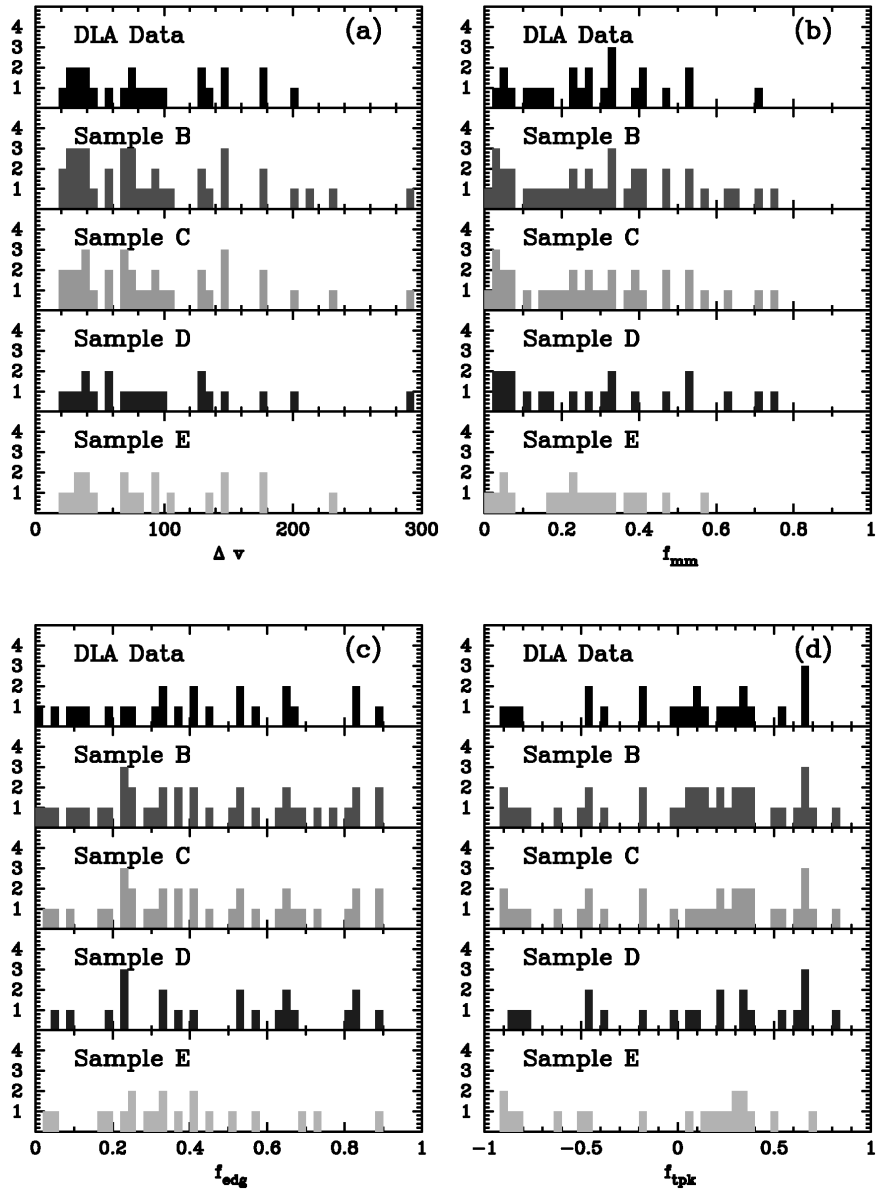


FIG. 4.—Statistical test distributions ([*a*] velocity-interval, [*b*] mean-median, [*c*] edge-leading, and [*d*] two-peak) for data sample A (the 17 damped Lyα profiles from PW), sample B (the 31 profiles comprising the current data sample), sample C [27 of the current profiles that satisfy stricter $N$(H I) criteria], sample D (a low-redshift subsample), and sample E (a high-redshift subsample).

described by the WRP4 model (see Table 4) and has a large impact parameter. The column density derived for this sight line is $N(\mathrm{H\ I}) = 1.6 \times 10^{21}$ cm$^{-2}$, and the resulting profile is plotted in the lower right panel. Note that this system would have $N(\mathrm{H\ I}) < 2 \times 10^{20}$ cm$^{-2}$ for all of the other lines of nodes considered here and would therefore not contribute to the test statistic distributions. The more common kinematic effect is illustrated in Figure 9*b*, where we plot a sight line doubly penetrating a disk from the WRP2 model. The resulting profile is significantly wider than if the disk were not warped.

TABLE 4

WARP PARAMETERS

| Label | $h/R_d$ | Line of Nodes | $R_H/R_d$ |
|---|---|---|---|
| WRP1..... | 0.2 | NULL | ... |
| WRP2..... | 0.2 | M33 | 2.0 |
| WRP3..... | 0.2 | CLON | 2.0 |
| WRP4..... | 0.2 | M83 | 2.0 |
| WRP5..... | 0.2 | CLON | 3.0 |
| WRP6..... | 0.3 | NULL | ... |
| WRP7..... | 0.3 | M83 | 2.0 |
| WRP8..... | 0.3 | CLON | 2.0 |

We performed a series of Monte Carlo simulations for warped disks with a variety of thicknesses, $R_H/R_d$ values, and lines of nodes. Figure 10 plots the $f_{\Delta v}$ distribution for eight representative warp models corresponding to the parameters listed in Table 4. All of the models assume a rotation speed of $v_{rot} = 250$ km s$^{-1}$ and a central column density, $N_\perp(0) = 10^{21.2}$ cm$^{-2}$. In general, warping yields a greater number of moderate $\Delta v$ values ($\Delta v \approx \frac{1}{2} v_{rot}$) and a few more large $\Delta v$ values. This is the case for the M33 and CLON lines of nodes (e.g., compare the null model, WRP1, with WRP2 and WRP3) where the results resemble those for a thicker disk. This is not true for all lines of nodes. Note the difference between the results for models WRP3 and WRP4, which correspond to the CLON and M83 lines of nodes, respectively. While both warps attain a tilt angle of

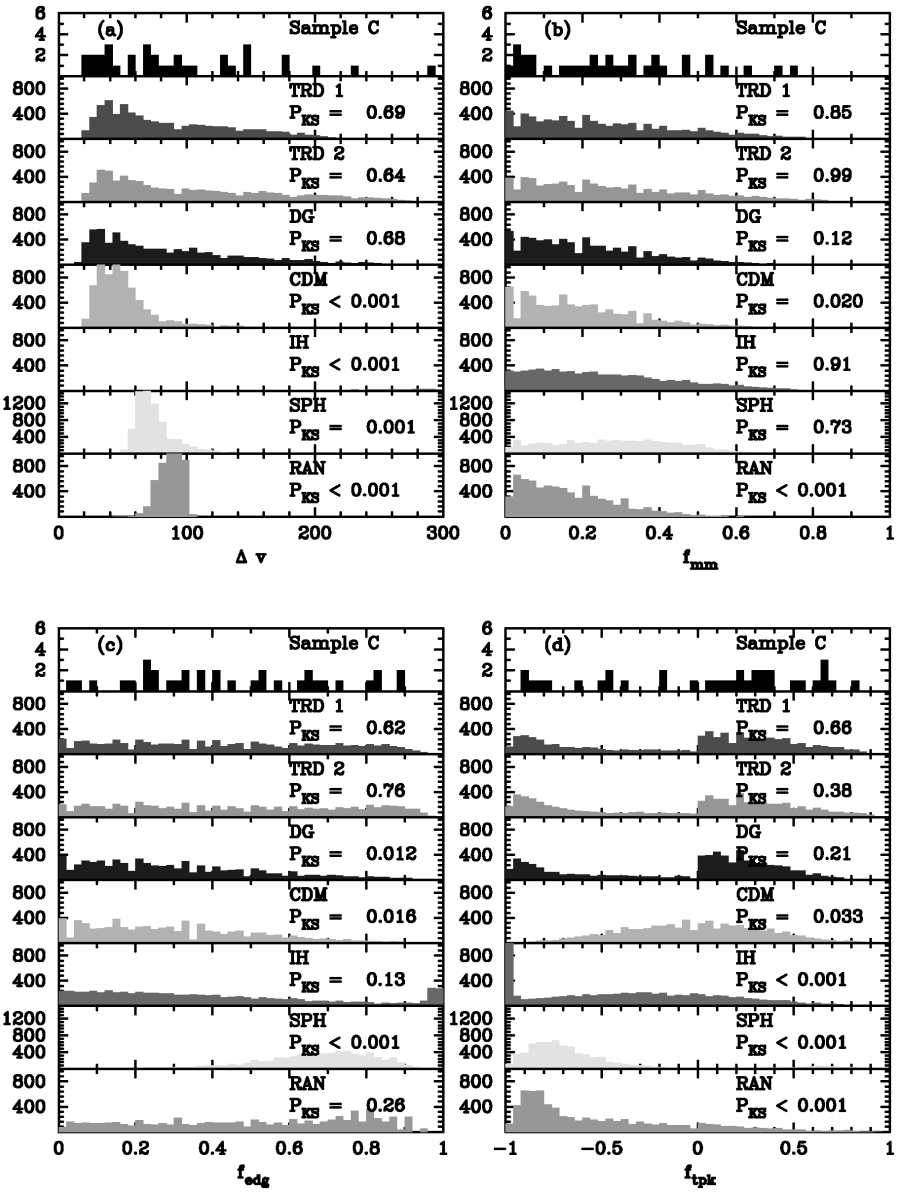


FIG. 5.—Statistical test distributions ([*a*] velocity-interval, [*b*] mean-median, [*c*] edge-leading, and [*d*] two-peak) for the models introduced in PW compared with sample C. Note that all the models that were ruled out in PW ($P_{KS} < 5\%$) are ruled out at even higher confidence levels now.

$\approx 40°$ at $R_H = 2R_d$, the M83 warp has a much larger cross section to sight lines satisfying the $N$(H I) criterion. As demonstrated in PW, those sight lines with large impact parameters tend to have smaller $\Delta v$, therefore the WRP4 model actually does more poorly than the unwarped disk, even though there are a number of sight lines that doubly penetrate the disk. The results are also sensitive to the adopted value of $R_H/R_d$. Comparing models WRP3 and WRP5, one notes the reduced effects of warping for larger $R_H/R_d$. As typical values of $R_H/R_d$ in local disks generally exceed 3, we expect warping to have even less of an effect on the $f_{\Delta v}$ distribution than that presented here. Curves WRP6–WRP8 demonstrate the results for warping for thicker disks. Qualitatively, the changes in the $f_{\Delta v}$ distribution are the same as those for the thinner disks.

To summarize, warping has only a moderate effect on the profile kinematics. For those lines of nodes where the dominant effect is of sight lines that penetrate the disk twice, warping mimics thicker disks, i.e., one observes a larger number of moderate $\Delta v$ values in the $f_{\Delta v}$ distribution. Furthermore, warping can also lead to significantly fewer moderate $\Delta v$ values when the cross section to the damped Ly$\alpha$ system extends to a higher impact parameter. This is the case for systems where the outer rings of the warp have $\beta \approx 180°$. Having performed simulations for a large range of $h$, $R_H/R_d$, and lines of nodes, we quantify the results as follows: (1) in extreme cases, warping mimics disks with up to 50% larger or smaller effective thickness ($h/R_d$ value), (2) warping leads to few additional large $\Delta v$ values in the $f_{\Delta v}$ distribution and therefore has little effect on the acceptable values for $v_{rot}$, and (3) we find that very thin ($h/R_d < 0.1$) warped disks are inconsistent with the damped Ly$\alpha$ observations.

### 4.2. *Rotation Curves*

In PW, the velocity field of the exponential disk model was given by $v_\phi = v_{rot}$, $v_R = v_Z = 0$, i.e., we assumed a flat rotation curve independent of radius and height above the

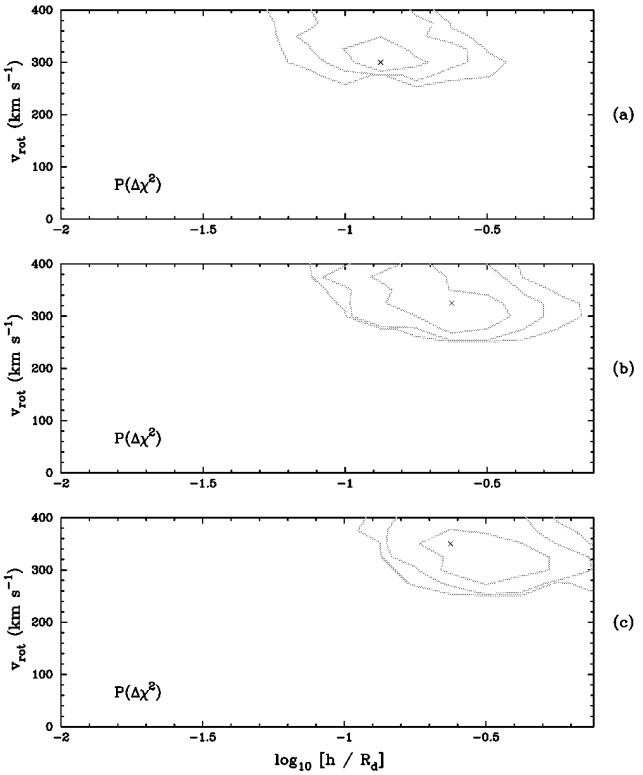


FIG. 6.—Isoprobability contours derived from the likelihood ratio test for the TRD model against the $f_{\Delta v}$ distribution from sample C with $N_\perp =$ (*a*) $10^{20.8}$ cm$^2$, (*b*) $10^{21.2}$ cm$^2$, and (*c*) $10^{21.6}$ cm$^2$. Contour levels are drawn at $P = 0.01$, 0.05, and 0.32. Note that the $f_{\Delta v}$ distribution would imply rotation speeds $v > 250$ km s$^{-1}$ given the assumption of a single population of disks.

midplane of the disk. This is a good zeroth-order representation for the rotation curve of spiral disks at large radii. But it breaks down at small radii because of the singularity implied for the mass density at $R = 0$. In more realistic models the density approaches a finite central value at $R$ less than some core radius, resulting in $v_\phi = 0$ at $R = 0$. The independence of $v_\phi$ with $Z$ may also be unrealistic. In their analysis of the kinematics of the ionized gas associated with C IV absorption lines, Savage, Sembach, & Lu (1997) find evidence that $v_\phi = v_{\rm rot}$ up to $|Z| \approx 5$ kpc above midplane. On the other hand, (R. Sancisi 1998, private communication) finds evidence for a decrease in $v_\phi$ with increasing $|Z|$ in his H I studies of edge-on spirals. In fact, unless there is strong coupling between layers of adjacent $Z$, this is what one expects. Therefore, a more physical rotation curve will (1) approach $v_{\rm rot} = 0$ km s$^{-1}$ at $R = 0$ where the enclosed mass density presumably approaches a finite value and (2) likely decrease in speed with increasing height above the midplane. In this section, we consider a range of rotation curves appropriate for a system comprising a thick disk, bulge, and dark matter halo.

#### 4.2.1. *Thick Disk*

As demonstrated in PW (reaffirmed in § 3.2), the kinematics of the damped Lyα systems are consistent with thick rotating disks. Furthermore, we showed that the vertical scale height, $h$, must be greater than one-tenth of the radial scale length, $R_d$. Therefore, the thin–disk approximation is not applicable for deriving the rotation curve of these disks. In this section, we detail a numerical solution for the rotation curve of a thick disk by explicitly solving Poisson's equation and combining the solution with the condition for centrifugal equilibrium.

##### 4.2.1.1. The Fourier-Bessel Transformation Method

Our approach is an extension of the technique developed by Toomre (1963) for the thin-disk solution and more recently applied by Casertano (1983) to the rotation curve for a thick disk at midplane. We calculate the disk potential by Fourier-Bessel–transforming Poisson's equation,

$$\nabla^2\Phi = 4\pi G\rho \ . \tag{5}$$

We adopt an exponential mass density of the form

$$\rho(R, Z) = \rho_0 \exp(-R/R_d) \exp(-|Z|/h) \ , \tag{6}$$

where $\rho_0$, the central mass density, is related to the central surface density, $\Sigma_0$, and central H I column density, $N_\perp(0)$, by

$$\rho_0 = \frac{\Sigma_0}{2h} = \mu m_p \frac{N_\perp(0)}{2h} \ , \tag{7}$$

with $\mu$ the molecular weight relative to hydrogen. This relation implicitly assumes that the mass of the disk is dominated by H I gas, i.e., we ignore any contribution from stars or molecular hydrogen.

Taking the Fourier-Bessel transformation of Poisson's equation, we find

$$\tilde{\Phi}(k, Z) = \frac{-2\pi G}{k} \int_{-\infty}^{+\infty} \exp(-k|Z - \zeta|)\tilde{\rho}(k, \zeta)d\zeta \ , \tag{8}$$

where

$$\tilde{\rho}(k, \zeta) = \rho_0 \exp\left(\frac{-|\zeta|}{h}\right) \int_0^\infty J_0(kR) \exp\left(-\frac{R}{R_d}\right) R\, dR \ . \tag{9}$$

This integral is analytic (Gradshteyn & Ryzhik 1980, 6.623, eq. [2]):

$$\tilde{\rho}(k, \zeta) = \frac{2R_d^{-1}\Gamma(3/2)\rho_0}{\sqrt{\pi}(R_d^{-2} + k^2)^{3/2}} \exp\left(\frac{-|\zeta|}{h}\right) . \tag{10}$$

Evaluating $\tilde{\Phi}(k, Z)$, we find

$$\tilde{\Phi}(k, Z) = \frac{A}{k(R_d^{-2} + k^2)^{3/2}} \left\{ \frac{1}{hk + 1} \left[ \exp\left(-\frac{Z}{h}\right) + \exp(-kZ) \right] + \frac{1}{hk - 1} \left[ \exp\left(-\frac{Z}{h}\right) - \exp(-kZ) \right] \right\} . \tag{11}$$

where the constant $A$ is

$$A = \frac{G\pi\Sigma_0}{R_d} \ . \tag{12}$$

Finally, we take the inverse transform of $\tilde{\Phi}$,

$$\Phi(R, Z) = \int_0^\infty J_0(kR)\tilde{\Phi}(k, Z)k\, dk \ . \tag{13}$$

The thick-disk rotation curve is therefore given by

$$v_\phi^2|_{\rm disk}(R, Z) = -R \frac{\partial}{\partial R} \Phi(R, Z) = R \int_0^\infty J_1(kR)\tilde{\Phi}(k, Z)k^2\, dk \ , \tag{14}$$

which can be evaluated very accurately with standard numerical techniques. As the value for $\Sigma_0$ derived from the

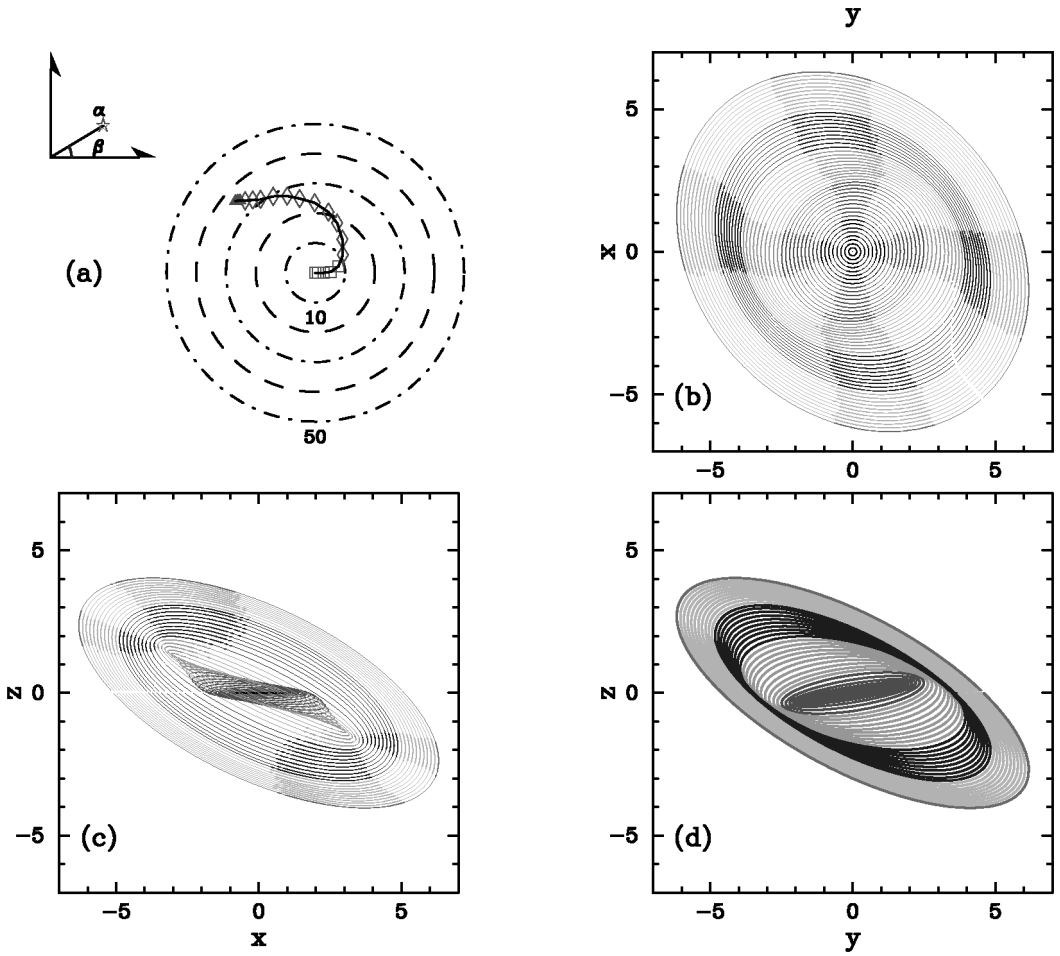


FIG. 7.—The polar plot depicts the line of nodes for a warped disk. Each successive point on the solid line indicates rings of monotonically increasing radii. The azimuthal angle ($\beta$) indicates the rotation angle of the ring, and the "radial" angle ($\alpha$) designates the tilt angle of the ring. The remaining plots show the warped disk as a series of rings viewed three perspectives.

damped Ly$\alpha$ observations (i.e., $N_\perp(0)$) is significantly lower than that observed in present galaxies, the disk rotation curve will peak at $v_{\rm max} \ll 200$ km s$^{-1}$ ($v_\phi^2 \propto \Sigma_0 R_d$) unless the H I gas contributes only a small fraction ($< 30\%$) of the disk mass. While it is possible that stars may double the surface density in the inner part of the disk (see Wolfe & Prochaska 1998), we proceed under the assumption that the H I gas dominates.

#### 4.2.1.2. Thick-Disk Curves

Figure 11 shows the rotation curve at midplane, $v_\phi(R, 0)$, derived from equation (14) for five disks with varying thickness. Also plotted is the rotation curve derived with the thin-disk approximation, normalized to have the same maximum rotation speed as the curve with $h/R_d = 1 \times 10^{-5}$. These two curves are in such close agreement that they are indistinguishable in Figure 11, verifying the accuracy of the numerical solution. Note that all of the other curves are normalized to have the same central column density, $N_\perp(0)$. Physically this normalization implies very different central mass densities for the different thickness disks [$\rho_0 \propto N_\perp(0) h^{-1}$]. There is a decrease in $v_\phi$ with increasing $h/R_d$, as expected, because $\rho_0$ is smaller and therefore the centrifugal force is smaller at a given radius $R$. Even for $h/R_d = 0.3$; however, the resulting rotation curve nearly traces that for the thin disk.

The rotation curve at various heights in a disk with $h/R_d = 0.3$ is plotted in Figure 12. Note that the curves at $Z = 1.67h$ and at midplane differ by less than 10%, and even at $Z = 6.67h$ there is generally less than a 50% effect. We find similar results for disks of all thicknesses. Since nearly all of the gas arises within $\approx 2\ h$ of the midplane, in general we expect the decrease in $v_\phi$ with increasing $Z$ to have little effect on the kinematic results. In fact, it is possible that the decrease in $v_\phi$ will actually increase the differential rotation along a given sight line.

### 4.2.2. *Bulge and Halo*

For the bulge rotation curve we assume the Hernquist bulge model (Hernquist 1990) parameterized by the peak velocity, $v_b$, and core radius, $R_b$:

$$v_{\rm circ}^2|_{\rm bulge}(r) = 4v_b^2 \frac{rR_b}{(r + R_b)^2}, \quad (15)$$

where we can relate $v_b$ and $R_b$ to the bulge mass, $M_b$, by the following expression:

$$M_b = 2.7 \times 10^9\ M_\odot \left(\frac{v_b}{200\ {\rm km\ s^{-1}}}\right)^2 \left(\frac{R_b}{100\ {\rm pc}}\right). \quad (16)$$

Meanwhile, for the halo we require a density profile which yields a flat rotation curve at large radii. We adopt

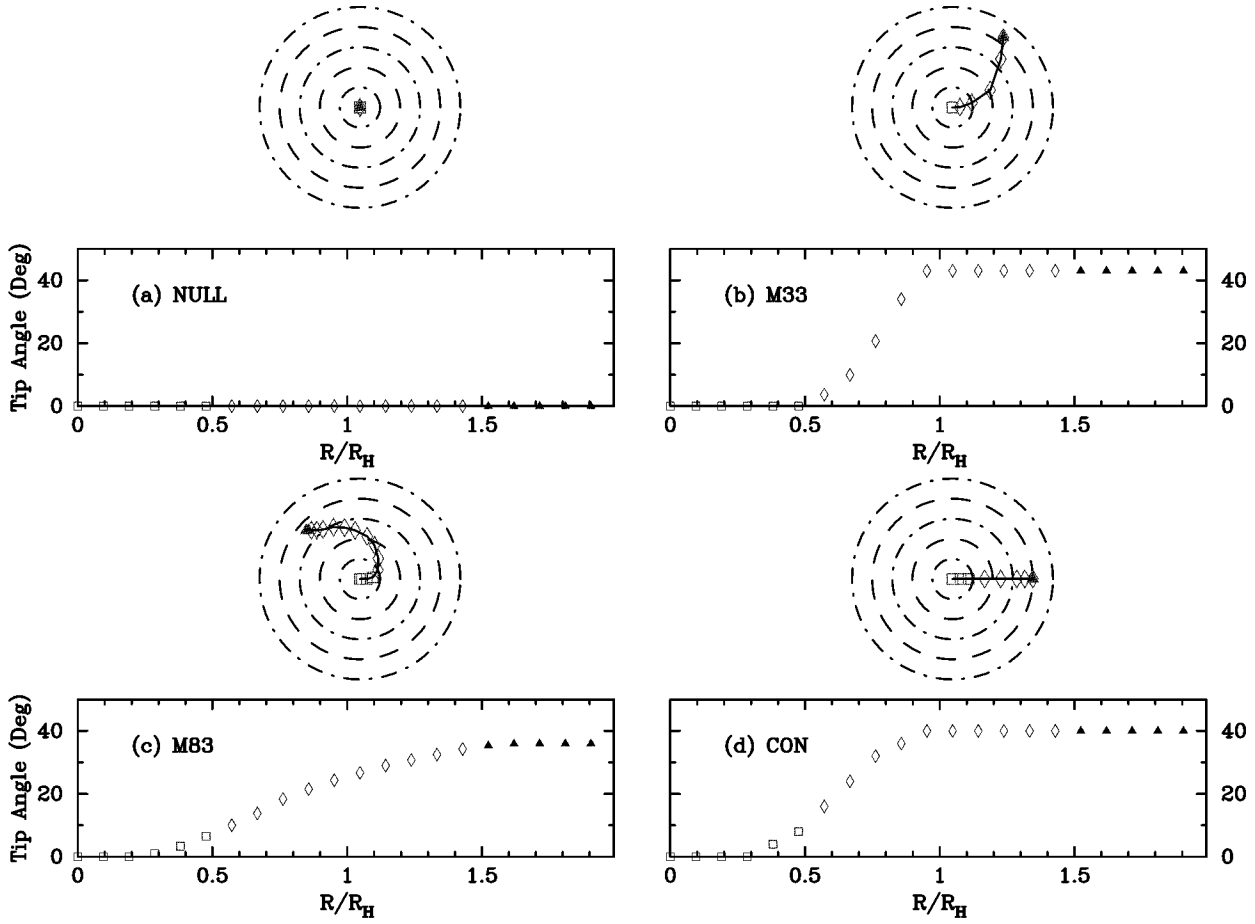


FIG. 8.—Lines of nodes for the four canonical warped disks: (*a*) an unwarped disk, (*b*) M33, (*c*) M83, and (*d*) an artificial warp. The polar plot has the same meaning as in Fig. 7. The *x*-*y* plot reveals the radial dependence of the tilt angle as a function of the effective Holmberg radius, $R_H$.

the following density profile,

$$\rho\,|_{\rm halo}(r) = \frac{\rho_h}{1 + (r/R_h)^2}\,, \tag{17}$$

where $\rho_h$ is the central density of the halo and $R_h$ is the core radius. This gives the following rotation curve,

$$v^2_{\rm circ}\,|_{\rm halo}(r) = v_h^2\left[1 - \frac{R_h}{r}\tan^{-1}\left(\frac{r}{R_h}\right)\right], \tag{18}$$

where $v_h$ is the halo rotation speed at large radii.

As both the bulge and halo are spherically symmetric, the rotation curves in cylindrical coordinates are

$$v_\phi^2\,|_{\rm bulge}(R, Z) = \frac{R^2}{\sqrt{R^2 + Z^2}}\,\frac{4v_b^2\,R_b}{(\sqrt{R^2 + Z^2} + R_b)^2} \tag{19}$$

and

$$v_\phi^2\,|_{\rm halo}(R, Z) = v_h^2\,\frac{R^2}{R^2 + Z^2} \times\left[1 - \frac{R_h}{\sqrt{R^2 + Z^2}}\tan^{-1}\left(\frac{\sqrt{R^2 + Z^2}}{R_h}\right)\right]. \tag{20}$$

#### 4.2.3. *Results*

The disk rotation curve is uniquely parameterized by $h$ and $\Sigma_0$, where $h$ and all other distance scales are in units of the radial scale length, $R_d$, and $\Sigma_0$ is the disk surface density at $R = 0$. The bulge and halo models are each parameterized by two variables that describe the slope of the curve ($R_b$, $R_h$) and the maximum rotation speed ($v_b$, $v_h$) at $Z = 0$. The total rotation speed, then, is given by

$$v_\phi^2\,|_{\rm tot}(R, Z) = v_\phi^2\,|_{\rm halo}(R, Z) + v_\phi^2\,|_{\rm bulge}(R, Z) + v_\phi^2\,|_{\rm disk}(R, Z)\,. \tag{21}$$

We have performed simulations for a wide range of the six parameters. The main results of the analysis are presented in Figure 13, and the rotational parameters are given in Table 5. Also listed is the peak rotation speed of each rotation curve, $v_{\rm max}$. For all of the models presented here we assume $N_\perp(0) = 10^{21.2}$ cm$^{-2}$ and that $h/R_d = 0.3$.

To facilitate a direct comparison with the TRD model, we plot the results for a flat rotation curve with $v_{\rm max} = 250$ km s$^{-1}$. For a given value of $v_{\rm max}$, the flat rotation curve yields a greater fraction of large velocity widths than any other rotation curve. Therefore, it gives the best agreement with the empirical distribution provided $v_{\rm max} \lesssim 350$ km s$^{-1}$, above which the distribution has too many large $\Delta v$ values. For model CRV2 (see Table 5), we assume a thick disk with $\Sigma_0 = \mu m_p N_\perp(0) = 18\ M_\odot$ pc$^{-2}$ and $R_d = 10$ kpc, which implies $v_{\rm max} = 41$ km s$^{-1}$. This model corresponds to $N_\perp(0) = 10^{21}$ cm$^{-2}$ as inferred from the damped Lyα observations. The value of $R_d$ was chosen to correspond roughly to the cross section derived for damped Lyα systems assuming a number density approximately equal to that for spiral galaxies in the present epoch (Wolfe et al. 1995). As noted above and shown in Figure 13, the mass associated with the H I disk implies a rotation curve that is inconsis-

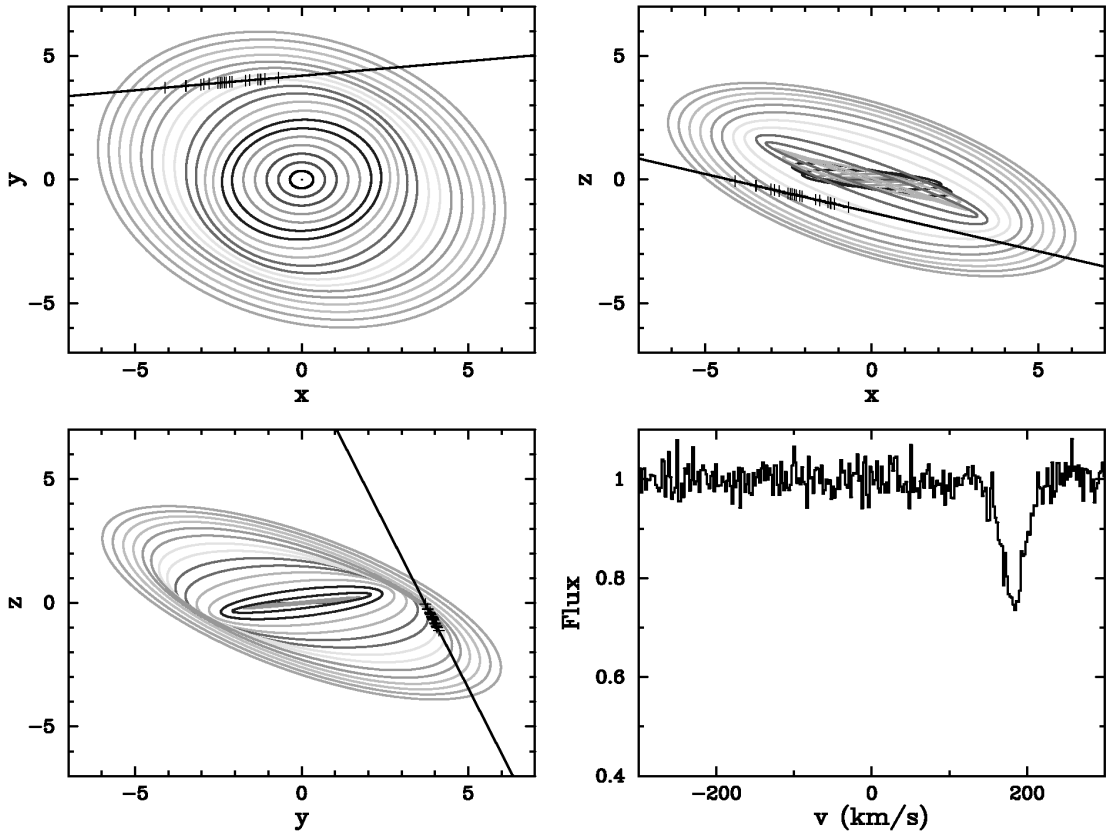


FIG. 9*a*

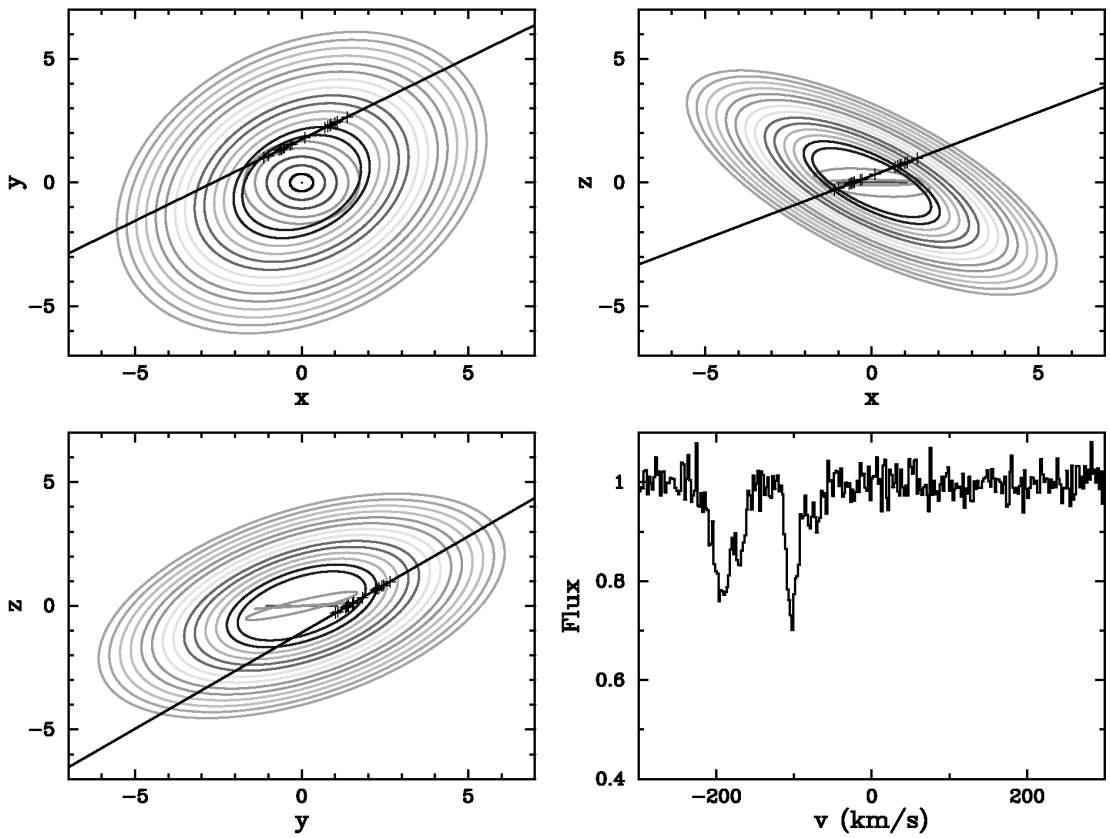


FIG. 9*b*

FIG. 9.—Illustration of the two principal kinematic effects associated with warped disks: (*a*) a sight line with large impact parameter yielding a small $\Delta v$ which would not be included in a treatment of an unwarped disk, as $N$(H I) would be less than $N_{\rm thresh}$; (*b*) a sight line doubly penetrating the disk, resulting in a significantly larger $\Delta v$ than if the disk were not warped. The plus signs indicate the position of clouds along the sight line.

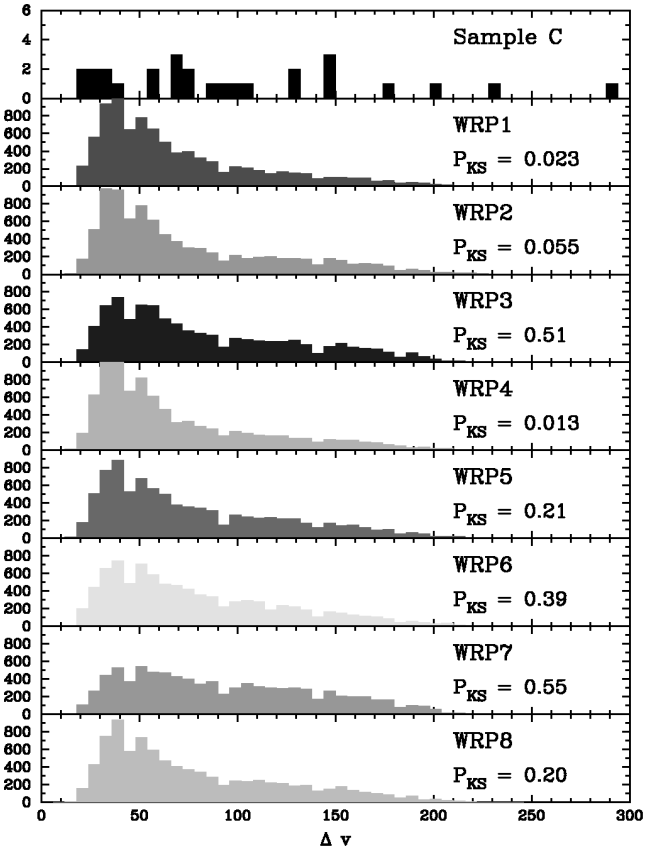


FIG. 10.—The $f_{\Delta v}$ distribution for eight warp models compared with that for sample C. The results demonstrate that warping has only a minor effect on the TRD model.

tent with the damped Lyα observations. The results for the CRV3 model demonstrate that a disk with $\Sigma_0 = 1440\ M_\odot$ pc$^{-2}$ and $R_d = 5$ kpc is consistent, yet this implies that less than 95% of the disk mass is in a component other than H I gas. It is unlikely that $\Sigma_0$ approaches even 500 $M_\odot$ pc$^{-2}$ given current estimates of the stellar (Wolfe & Prochaska 1998) and molecular (Ge & Bechtold 1997) baryonic fraction. Furthermore, if $\Sigma_0 \approx 1500\ M_\odot$ pc$^{-2}$ in every damped system, this would imply a comoving density approximately 100 times that of visible matter in the present universe. On the other hand, if we include a massive dark halo ($v_h = 250$ km s$^{-1}$), the resulting $f_{\Delta v}$ distribution (CRV4) is consistent with the empirical distribution provided that $R_h/R_d \lesssim 1$. For larger values of $R_h/R_d$, the rotation curve (CRV5) rises too slowly to yield large $\Delta v$. Finally, we investigate the effect of including a massive bulge in models CRV6 and CRV7, where we adopt the same disk and halo curves from models CRV4 and CRV5. We find that the presence of a massive bulge ($v_b = 180$ km s$^{-1}$) with $R_b \ll R_d$ has little impact on the $f_{\Delta v}$ distribution, as the bulge affects only the inner rotation curve. To conclude, the TRD model requires a rotation curve which is nearly flat for $R_d > 1$. While this can be achieved with a massive disk resembling that of the Milky Way, it would requires a nongaseous baryonic component with comoving density 2 orders of magnitude greater than the density of visible matter in current galaxies, which is implausible. Assuming that the mass of the disk is dominated by the H I gas with $N_\perp(0) \approx 10^{21}$ cm$^{-2}$ requires the presence of a massive dark halo with $R_h \lesssim R_d$.

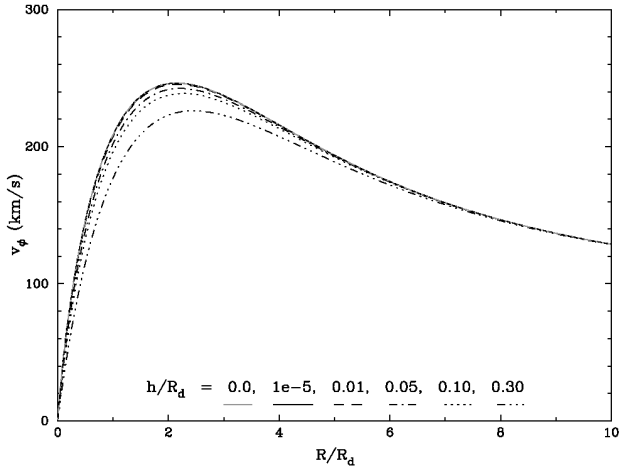


FIG. 11.—Rotation curve at midplane, $v_{\rm circ}(R, 0)$, for five disks with varying thickness, $h/R_d$. All of the curves are normalized to have the same central column density $N_\perp(0)$. There is only small dependence on thickness for the rotation curves.

### 4.3. *Photoionization*

Over the redshift range spanning our damped Lyα observations the intergalactic medium (IGM) is primarily ionized, presumably by the ambient UV radiation field from background quasars. At redshift $z \sim 2.5$ the UV intensity is often described as a modified power law (Haardt & Madau 1996):

$$J(\nu) \approx J_{912}\left(\frac{\nu}{\nu_{912}}\right)^{\alpha} \qquad (22)$$

with exponent $\alpha \approx -1$ and $J_{912} \approx 10^{-21.5}$ ergs s$^{-1}$ cm$^{-2}$ sr$^{-1}$ Hz$^{-1}$. This background flux creates ionization fronts in the H I disks comprising the TRD model, analogous to those observed in present spiral galaxies (Maloney 1993). Because a complete treatment involving a solution of the radiative transfer equation is beyond the scope of this paper, we address the problem with two different approximations. In one case, we assume a sharp H I edge to the disks of the TRD model. In the other, we assume the gas is photoionized if its volume density is below some critical value. The photoionization of the disk will eliminate from the derived statistical sample those sight lines with

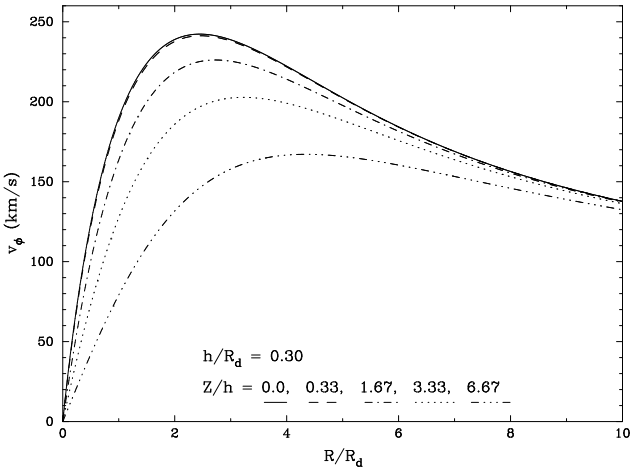


FIG. 12.—Rotation curves for a disk with $h/R_d = 0.3$ at various heights within the disk.

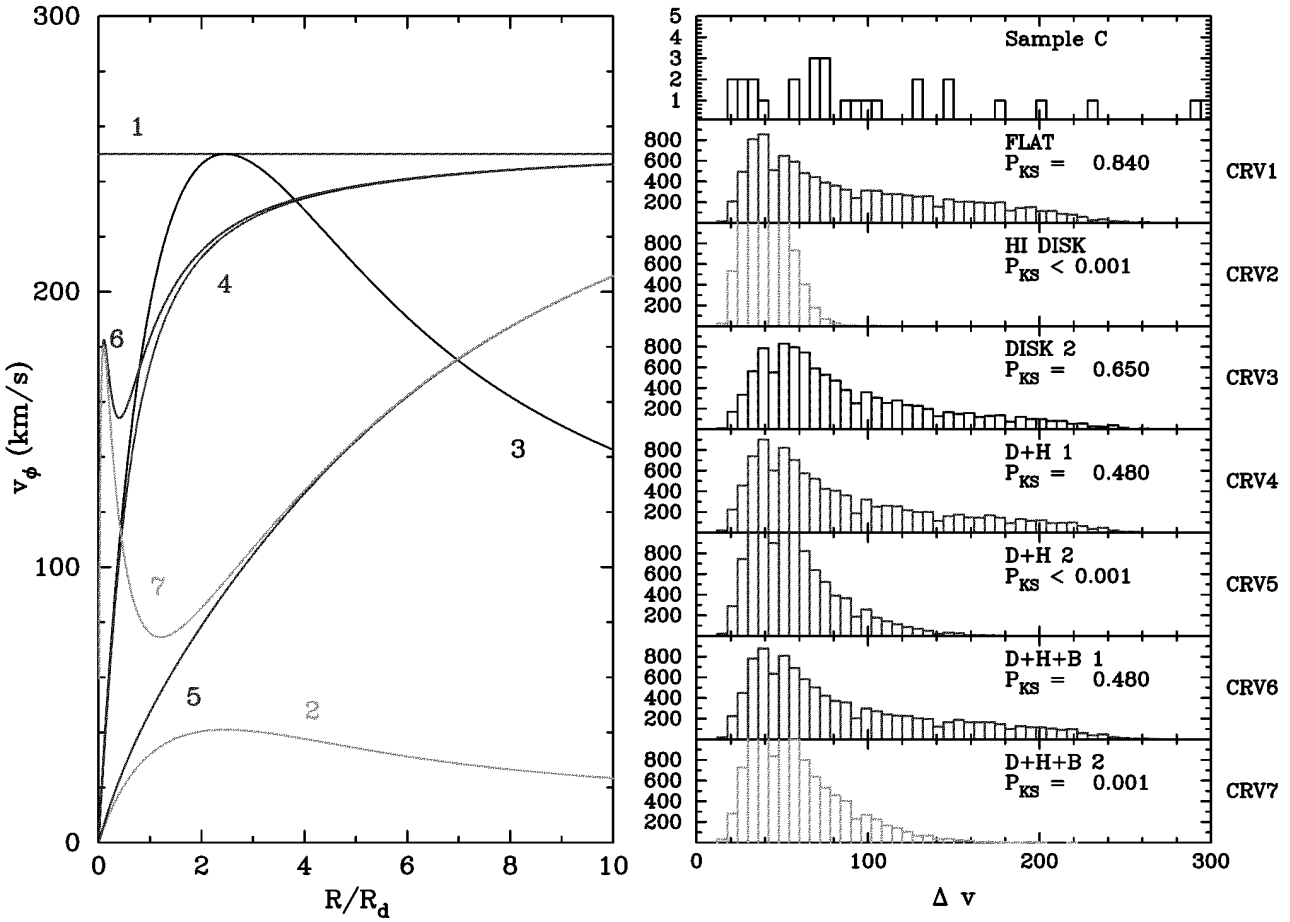


FIG. 13.—*Left*: Rotation curve at midplane for disks with varying bulge, halo, and disk components. *Right*: $f_{\Delta v}$ distributions for the eight curves compared against sample C.

$N(\mathrm{H\ I}) \approx N_{\mathrm{thresh}}$. Since these sight lines tend to penetrate the disk at large impact parameters that yield small $\Delta v$, we predict a general shift in the $f_{\Delta v}$ distribution to larger velocity widths. By analogy to the results from warped disk models, we expect the photoionized disk to mimic thicker disks.

First, we consider the H I edge model, which incorporates a sharp "H I edge" for the exponential disk at a column density, $N_{\mathrm{ph}}$. Using a two-dimensional analogy to the Strömgren sphere argument, we find that the column density of ionized gas above the H I gas is given by

$$N_{\mathrm{ph}} = \frac{2\phi}{\alpha_{\mathrm{rec}}\langle n\rangle}, \tag{23}$$

where $\phi$ is the flux of ionizing photons (i.e., $\phi = \int_{\nu_{\mathrm{H}}}^{\infty} d\nu\, 2\pi J_\nu/h\nu$), $\langle n\rangle$ is the average hydrogen volume density, and $\alpha_{\mathrm{rec}}$ is the case B recombination coefficient. Given the above value for $J_{912}$, with $\langle n\rangle = 1\ \mathrm{cm}^{-3}$ we find $N_{\mathrm{ph}} \approx 10^{18}\ \mathrm{cm}^{-2}$. To simulate photoionization of the H I disks in the TRD model, we systematically remove $N_{\mathrm{ph}}$ of column normal to the disk everywhere. This leads to a sharp H I edge at $R_{\mathrm{ph}} = \ln[N_\perp(0)/2N_{\mathrm{ph}}]$ and effectively removes $2N_{\mathrm{ph}}$ from each sight line that penetrates within $R_{\mathrm{ph}}$. As $J_{912}$ is poorly constrained observationally, we consider $J_{912}$ values ranging from $10^{-21.0}$ to $10^{-22.5}$ ergs$^{-1}$ cm$^{-2}$ sr$^{-1}$ Hz$^{-1}$, where the favored value is $10^{-21.5}$ (Haardt & Madau 1996). To consider meaningful $N_{\mathrm{ph}}$ values, we relate $N_{\mathrm{ph}}$ to $N_\perp(0)$, $h$, and $J_{912}$ with the following equation:

$$N_{\mathrm{ph}} = 10^{19}\ \mathrm{cm}^{-2}\left(\frac{h/R_d}{0.2}\right)\left(\frac{J_{912}}{10^{-21.5}}\right)\left[\frac{10^{21.2}}{N_\perp(0)}\right]. \tag{24}$$

TABLE 5

ROTATION CURVES

| CRV | $v_{\mathrm{disk}}^{\mathrm{max}}$ (km s$^{-1}$) | $\Sigma$ ($M_\odot$ pc$^{-2}$) | $v_b$ (km s$^{-1}$) | $R_b$ ($R_d$) | $v_h$ (km s$^{-1}$) | $R_h$ ($R_d$) | Comment |
|---|---|---|---|---|---|---|---|
| 1..... | 250 | ... | ... | ... | ... | ... | FLT |
| 2..... | 41 | 18 | ... | ... | ... | ... | Damped Lyα disk |
| 3..... | 250 | 1450 | ... | ... | ... | ... | Massive disk |
| 4..... | 250 | 18 | ... | ... | 250 | 0.5 | DSK + HLO 1 |
| 5..... | 250 | 18 | ... | ... | 250 | 5.0 | DSK + HLO 2 |
| 6..... | 250 | 18 | 180 | 0.1 | 250 | 0.5 | DSK + HLO + BLG 1 |
| 7..... | 250 | 18 | 180 | 0.1 | 250 | 5.0 | DSK + HLO + BLG 2 |

The other approximation we make to describe the photoionization of the disk is to assume the gas is predominantly ionized below a critical volume density, $n_{\rm ph}$. For the TRD model, the critical density can be defined as

$$n_{\rm ph} = n(R = R_{\rm ph}, Z = 0) = \frac{N_{\rm ph}}{h} \qquad (25)$$

with $R_{\rm ph}$ and $N_{\rm ph}$ defined as above. With $h = 0.3R_d$, $R_d = 5$ kpc, and $N_{\rm ph} = 10^{18}$–$10^{20}$ cm$^{-2}$, this implies density cutoffs of $n_{\rm ph} \approx 10^{-4}$ to $10^{-2}$ cm$^{-3}$. We refer to this photoionization model as the "critical density" model.

It is revealing to examine the kinematic characteristics of those sight lines *removed* from the TRD statistical sample on account of photoionization. Figure 14 plots the test statistics for the *eliminated* sight lines from four representative runs of each photoionization model, the parameters of which are given in Table 6. Included in each panel of the $f_{\Delta v}$ distribution is the percentage of sight lines eliminated. Note that very few sight lines are removed in a 10,000 sight-line run for $N_{\rm ph} \approx 10^{18}$ cm$^{-2}$, hence the effects of photoionization are minimal for small $J_{912}$, larger $N_\perp(0)$, or small $h/R_d$. By contrast, simulations with $N_{\rm ph} = 10^{20}$ cm$^{-2}$ have very

TABLE 6

PHOTOIONIZATION MODELS

| Label | Model[a] | $h/R_d$ | log $N$(H I) | $-$log $J_{912}$ | log $N_{\rm ph}$ |
|---|---|---|---|---|---|
| PHT1..... | H I[b] | 0.3 | 21.2 | 22.0 | 18.7 |
| PHT2..... | H I | 0.3 | 21.2 | 20.5 | 20.2 |
| PHT3..... | H I | 0.3 | 20.8 | 21.5 | 19.6 |
| PHT4..... | H I | 0.1 | 21.2 | 21.0 | 19.2 |
| PHT5..... | CD[c] | 0.3 | 21.2 | 22.0 | 18.7 |
| PHT6..... | CD | 0.3 | 21.2 | 20.5 | 20.2 |
| PHT7..... | CD | 0.3 | 20.8 | 21.5 | 19.6 |
| PHT8..... | CD | 0.1 | 21.2 | 21.0 | 19.2 |

[a] All models assume $v_{\rm rot} = 225$ km s$^{-1}$.
[b] H I edge model.
[c] Critical density model.

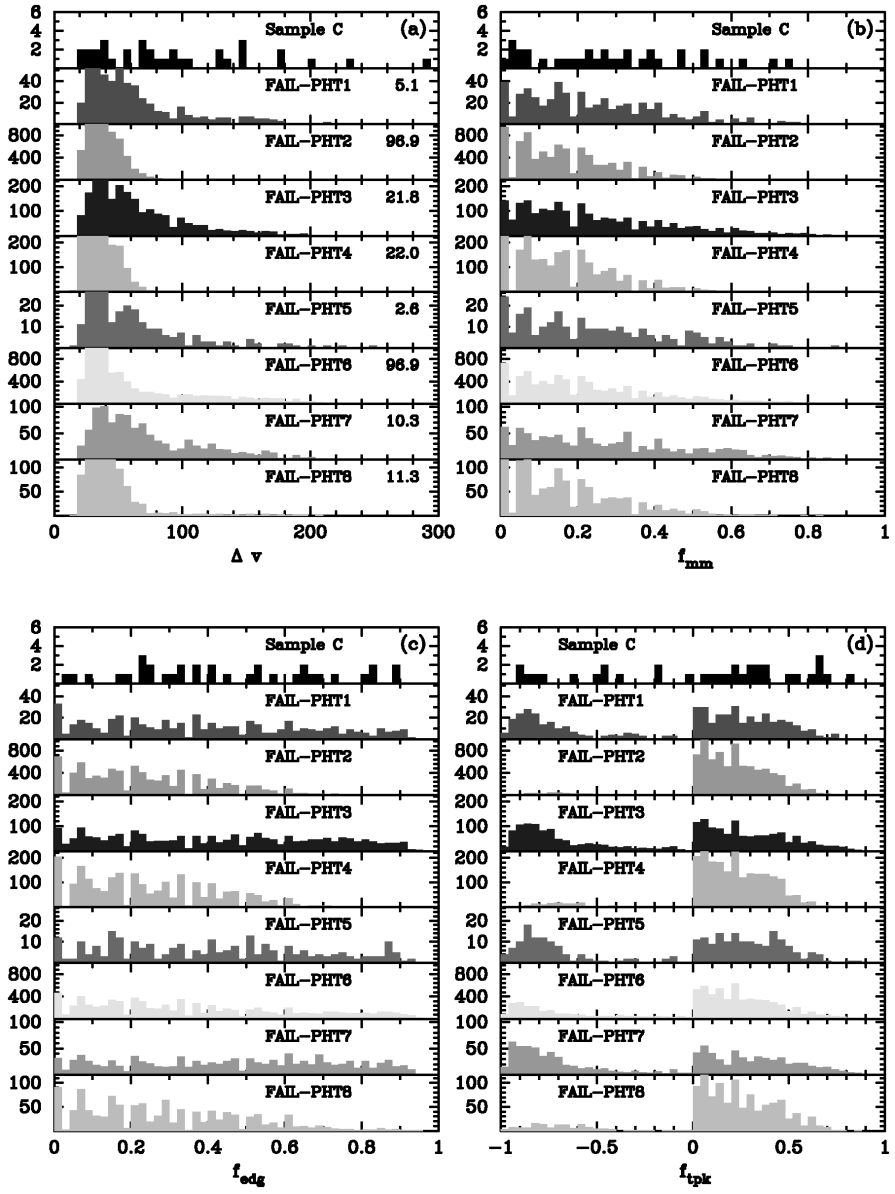


FIG. 14.—Test statistic distributions ([*a*] velocity-interval, [*b*] mean-median, [*c*] edge-leading, and [*d*] two-peak) for the *removed* sight lines from four representative runs of the two photoionization models considered in the text.

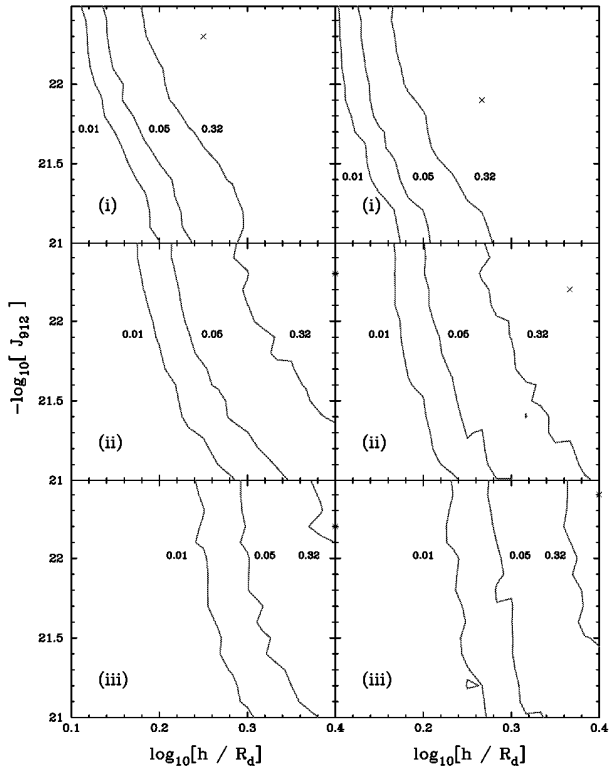


FIG. 15.—Isoprobability contours for disks with (i) $N_\perp = 10^{20.8}$ cm$^{-2}$, (ii) $N_\perp = 10^{21.2}$ cm$^{-2}$, and (iii) $N_\perp = 10^{21.6}$ cm$^{-2}$, for a range of $h/R_d$ and $J_{912}$ values in the H I edge model (*left*) and the critical density model (*right*).

many sight lines removed so that there is a large impact on the simulations. As expected, the vast majority of sight lines eliminated have small $\Delta v$ values and correspondingly small $f_{\rm mm}$ and $f_{\rm 2pk}$ values. Also, the results for thin disks are essentially unaffected by photoionization, as most sight lines yield small $\Delta v$ irrespective of photoionization. The results are very similar for the two photoionization models, although the critical density model does remove a few more large $\Delta v$ values.

The results presented in Figure 14 suggest that photoionization will improve the agreement between models with small thickness or low rotation speed (i.e., models with an $f_{\Delta v}$ distribution dominated by small $\Delta v$) and the empirical data set. However, besides eliminating sight lines with small $N$(H I), photoionization of the edges of the disks tends to lower the average $\Delta v$ for a given sight line; because of photoionization, the H I path along a given sight line is reduced, which reduces the differential velocity along the line of sight and on average lowers $\Delta v$. The net result is that photoionization actually worsens the agreement for disks of all thickness and central column density, contrary to our initial expectation. Figure 15 presents isoprobability $P_{\rm KS}(\Delta v)$ contours for disks with (i) $N_\perp(0) = 10^{20.8}$ cm$^{-2}$, (ii) $N_\perp(0) = 10^{21.2}$ cm$^{-2}$, and (iii) $N_\perp(0) = 10^{21.6}$ cm$^{-2}$, for a range of $h/R_d$ and $J_{912}$ values in the H I edge model (*left*) and the critical density model (*right*). The three contours correspond to $P_{\rm KS}(\Delta v)$ values of 0.01, 0.05, and 0.32 and the cross marks the highest $P_{\rm KS}(\Delta v)$ value in the explored parameter space. The agreement clearly worsens for increasing $J_{912}$ and decreasing $h/R_d$. If the UV background does have $J_{912} \approx 10^{-21}$, then photoionization will have a significant impact on the results derived for in the TRD model. In particular, the thickness would have to exceed $h/R_d > 0.2$ for disks with $N_\perp(0) = 10^{20.8}$ cm$^{-2}$ and 0.3 for disks with larger $N_\perp(0)$. While such large values for $J_{912}$ are unlikely, they are not ruled out by current observations. For $J_{912} \approx 10^{-21.5}$ the effect on the TRD model is moderate, generally requiring less than a 30% increase in the thickness of the disks.

Last, we examine how the photoionization models affect the distribution of $N$(H I), $\Delta v$ pairs. In PW (Fig. 13) we noted the rather poor concordance between the TRD model and the damped Ly$\alpha$ observations and suggested that photoionization may improve the agreement. Specifically, we expected photoionization to reduce the number of sight lines with small $\Delta v$ and small $N$(H I) and thereby improve the agreement with the damped Ly$\alpha$ observations. Figure 16 plots the $N$(H I), $\Delta v$ pairs from sample C (*large squares*) and the $N$(H I), $\Delta v$ pairs for four of the photoionization (PHT) models. The PHT1 and PHT5 models indicate the results without significant photoionization, while the PHT2 and PHT6 models highlight its effects. The $P_{\rm KS}$ values were derived from the two-dimensional Kolmogorov-Smirnov test (Press 1992). For the reasons discussed above, photoionization worsens the agreement between the TRD model and damped distributions. While models PHT2 and PHT6 are inconsistent at the 99% confidence level, it should, however, be noted that one can improve the concordance by considering a range of $v_{\rm rot}$ and $N_\perp(0)$ values. Also, as discussed in Wolfe & Prochaska (1998), the presence of many large $\Delta v$, small $N$(H I) pairs may indicate the presence of a "hole" in the inner region of the disk as observed in many local spirals.

## 5. SUMMARY AND CONCLUSIONS

We have presented new observations on the low-ion kinematics of the damped Ly$\alpha$ systems. The full sample of 31 profiles confirms the primary conclusions of PW: in particular, (1) models with kinematics dominated by random or symmetric velocity fields are inconsistent with the damped Ly$\alpha$ kinematics, (2) the TRD model, which consists of a population of thick, rapidly rotating disks at high $z$, naturally reproduces both the observed edge-leading asymmetry of the empirical profiles and the distribution of velocity widths, and (3) models incorporating centrifugally supported disks within the framework of the standard CDM cosmology are ruled out at high levels of confidence. In addition, a comparison of the kinematic properties of profiles of the highest redshift systems ($\bar{z} = 3.24$) with the lower redshift systems ($\bar{z} = 2.06$) reveals no significant evolution in the kinematics of the damped Ly$\alpha$ systems. This last observation may place strong constraints on scenarios of galaxy formation that predict significant evolution over this epoch.

At present there are two working models that explain the kinematic characteristics of the damped Ly$\alpha$ systems: (1) the TRD model and (2) merging protogalactic clumps in numerical simulations of the standard CDM cosmology (Haehnelt et al. 1997). In this paper we have focused on the TRD model. In particular, we have investigated the robustness of the model to including more realistic disk properties, specifically disk warping, physical rotation curves, and photoionization. Given the prevalence of warping in local disk galaxies, we considered its effects on the kinematics of the disks in the TRD model. We found that the results of warping are dominated by two competing effects. Sight lines

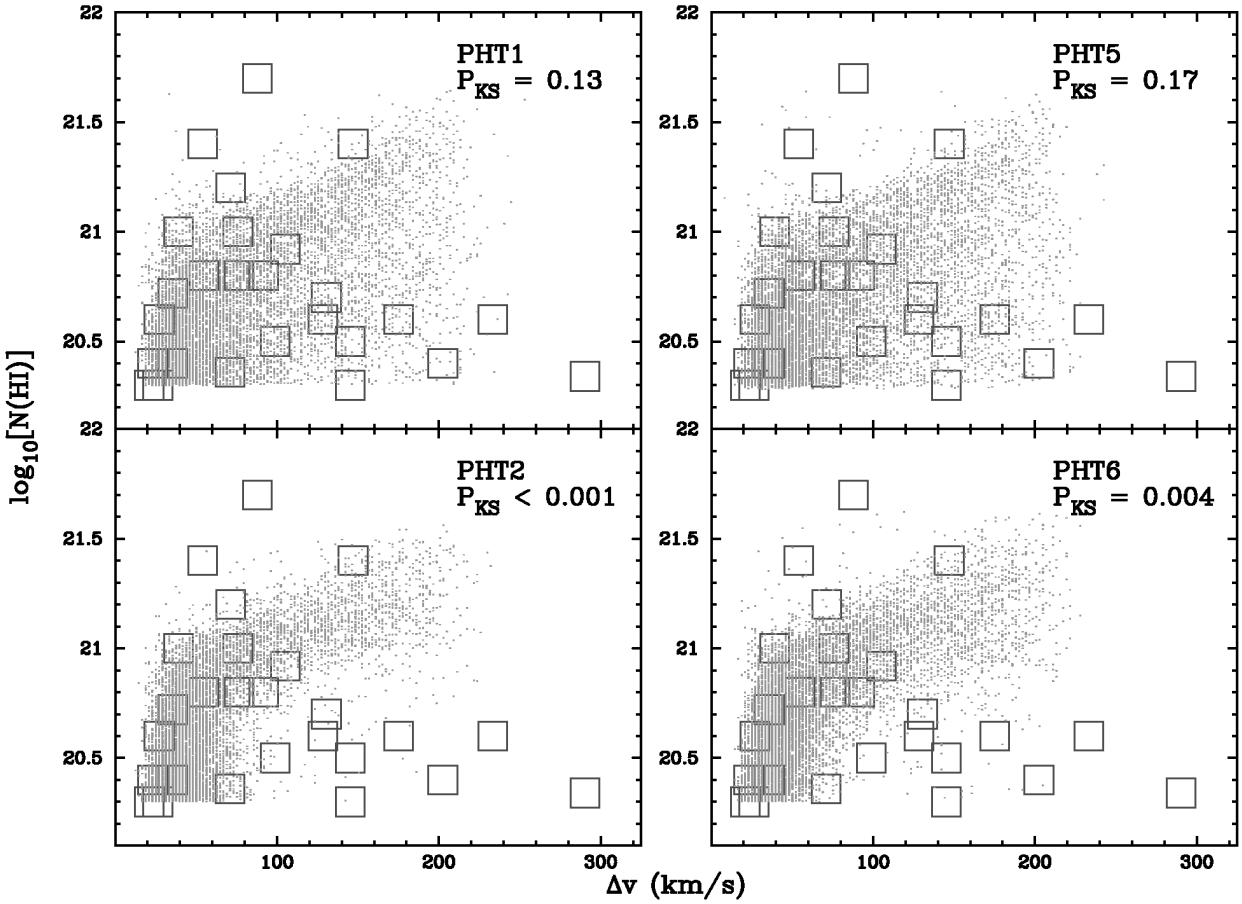


FIG. 16.—Plots of $N$(H I) vs. $\Delta v$ pairs for the damped Lyα systems (*squares*) and four photoionization models: PHT1 and PHT5 where $J_{912}$ is small and PHT2 and PHT6 where photoionization is significant. The $P_{KS}$ are derived from the two-dimensional KS test. Note that photoionization clearly worsens the agreement between the model and the empirical distribution.

that penetrate both the unwarped inner disk and the warped outer disk yield moderately higher $\Delta v$ than those simply intersecting an unwarped disk. At the same time, however, some warped disks have significantly larger cross section to sight lines with large impact parameters which tend to yield small $\Delta v$. Having considered a number of warped disks with a broad range of properties, we find that (1), in extreme cases, warping mimics disks with up to 50% larger or smaller effective thickness ($h/R_d$ value), (2) warping leads to very few extra large $\Delta v$ values in the $f_{\Delta v}$ distribution and therefore has little effect on the acceptable values for $v_{\rm rot}$, and (3) the lower limit to $h/R_d$ is nearly unchanged, as we find that $h$ must be greater than $0.1R_d$ for both warped and unwarped disks.

In PW, we assumed a flat rotation curve, $v_\phi = v_{\rm rot}$, extending from $R = 0 \rightarrow \infty$ and $Z = 0 \rightarrow \infty$. In this paper we adopted rotation curves derived from specific bulge, halo, and disk components. Assuming that an exponential profile is a good description of the density profile for the damped Lyα systems, we find the rotation curves derived from gravity generated by the H I gas *alone* cannot reproduce the empirical $f_{\Delta v}$ distribution. If the rotation curve is dominated by the disk, one must introduce another mass component (e.g., stars, molecules) to establish consistency. At the same time we find that the rotation curve derived from a massive halo with core radius $R_h \lesssim R_d$ also yields an $f_{\Delta v}$ distribution consistent with the observations. We believe that the latter explanation is more plausible. We also find the presence of the bulge to be largely inconsequential.

Last, we studied the effects of the intergalactic photoionizing background radiation on the disk kinematics. We made two separate approximations to model the photoionization of the disks: (*a*) an H I edge model where the disk is photoionized at radii $R > R_{\rm ph}$ with $R_{\rm ph}$ set by the intensity of the photoionizing background and the disk properties and (*b*) a critical density model where all gas with volume density $n \leq n_{\rm ph}$ is presumed ionized. Contrary to our expectations, we find that photoionization tends to worsen the agreement between the TRD model and the damped Lyα observations. The effect, however, is not large (<30%) for the favored value of $J_{912} = 10^{-21.5}$, but for $J_{912} = 10^{-21}$ a substantial (>50%) increase in the thickness of the disks would be required.

In summation, then, we find the TRD model is very robust to tests against the damped Lyα observations. The challenge remains, however, to consistently incorporate this model within a cosmological framework. While the clump model fits naturally within the SCDM cosmology, it must be demonstrated that the clump model exhibits similar robustness to comparisons with the damped Lyα kinematics. While Haehnelt et al. (1997) did show that the clump model could explain the damped Lyα observations from PW for a single set of parameters, a formal investigation of the full physical parameter space with meaningful statistics

has yet to be performed. In addition, it is not clear how that model will change given different cosmological parameters, e.g., an open universe where merging plays a smaller role at $z \approx 2.5$. The model must also be tested against the new observations, in particular the new $f_{\Delta v}$ distribution which extends to $\approx 300$ km s$^{-1}$. Finally, the fact that the numerical simulations do not reproduce the observed properties of modern galaxies when evolved to the present universe (Navarro, Frenk, & White 1995) suggests that the model may have serious inconsistencies in the early universe.

In future papers we will introduce observations of the high-ion transitions (e.g., C IV $\lambda$1548) with the aim of further constraining the two working models as well as advancing our understanding of the ionized gas associated with the damped Ly$\alpha$ systems. This gas is presumed to reside in the halo of these protogalaxies and therefore may give more direct indications of the dark matter associated with the damped Ly$\alpha$ systems. We also intend to consider effects (e.g., multiple disks) that would improve the agreement between the semianalytic models of standard cosmology (Kauffmann 1996; Mo, Mao, & White 1997).

We thank the group headed by W. L. W. Sargent, including Limin Lu, for generously providing us with their HIRES spectra. We also would like to thank R. Becker, S. Burles, L. Storrie-Lombardi, and I. Hook for providing targets. The authors would also like to thank Tom Barlow for his excellent HIRES data reduction software. Finally, we wish to acknowledge many helpful comments by the anonymous referee. A. M. W. and J. X. P. were partially supported by NASA grant NAGW-2119 and NSF grant AST 86-9420443.

## REFERENCES

Briggs, F. H. 1990, ApJ, 352, 15
Casertano, S. 1983, MNRAS, 203, 735
Eggen, O. J., Lynden-Bell, D., & Sandage, A. 1962, ApJ, 136, 748
Ge, J., & Bechtold, J. 1997, ApJ, 477, 73
Gradshteyn, I. S., & Ryzhik, I. M. 1980, Tables of Integrals, Series, and Products (New York: Academic)
Haardt, F., & Madau, P. 1996, ApJ, 461, 20
Haehnelt, M. G., Steinmetz, M., & Rauch, M. 1997, preprint (astro-ph 9706201)
Hernquist, L. 1990, ApJ, 356, 359
Jedamzik, K., & Prochaska, J. X. 1998, MNRAS, in press (astro-ph 9706290)
Kauffmann, G. 1996, MNRAS, 281, 475
Maloney, P. 1993, ApJ, 414, 41
Mo, H. J., Mao, S., & White, S. D. M. 1997, preprint (astro-ph/9707093)
Navarro, J. F., Frenk, C. S., & White, S. D. M. 1995, MNRAS, 275, 56
Press, W. H. 1992, Numerical Recipes in FORTRAN (New York: Cambridge Univ. Press)
Prochaska, J. X., & Wolfe, A. M. 1997, ApJ, 486, 73 (PW)
Savage, Sembach, & Lu, L. 1997,
Toomre, A. 1963, ApJ, 138, 385
Wolfe, A. M. 1995, in ESO Workshop on QSO Absorption Lines, ed. G. Meylan, (Berlin: Springer), 13
Wolfe, A. M., Lanzetta, K. M., Foltz, C. B., & Chaffee, F. H. 1995, ApJ, 454, 698
Wolfe, A. M., & Prochaska, J. X. 1998, ApJ, 494, L15